The Astronomical Journal, 164:39 (20pp), 2022 August https://doi.org/10.3847/1538-3881/ac7218

The Airborne Infrared Spectrometer: Development, Characterization, and the 2017 August 21 Eclipse Observation

Jenna E. Samra[1], Vanessa Marquez[1], Peter Cheimets[1], Edward E. DeLuca[1], Leon Golub[1], James W. Hannigan[2], Chad A. Madsen[1], Alisha Vira[3], and Arn Adams[4]
[1] Smithsonian Astrophysical Observatory, 60 Garden Street, Cambridge, MA 02138, USA; jsamra@cfa.harvard.edu
[2] Atmospheric Chemistry Observations and Modeling, National Center for Atmospheric Research, P.O. Box 3000, Boulder, CO 80307, USA
[3] Georgia Institute of Technology, 225 North Avenue, Atlanta, GA 30332, USA
[4] IRCameras, 30 S. Calle Cesar Chavez, Santa Barbara, CA 93103, USA
Received 2021 June 22; revised 2022 April 30; accepted 2022 May 20; published 2022 July 6

Abstract

On 2017 August 21, the Airborne Infrared Spectrometer (AIR-Spec) observed the total solar eclipse at an altitude of 14 km from aboard the NSF/NCAR Gulfstream V research aircraft. The instrument successfully observed the five coronal emission lines that it was designed to measure: Si X 1.431 μm, S XI 1.921 μm, Fe IX 2.853 μm, Mg VIII 3.028 μm, and Si IX 3.935 μm. Characterizing these magnetically sensitive emission lines is an important first step in designing future instruments to monitor the coronal magnetic field, which drives space weather events, as well as coronal heating, structure, and dynamics. The AIR-Spec instrument includes an image stabilization system, feed telescope, grating spectrometer, and slit-jaw imager. This paper details the instrument design, optical alignment method, image processing, and data calibration approach. The eclipse observations are described and the available data are summarized.

Unified Astronomy Thesaurus concepts: Solar coronal lines (2038); Solar instruments (1499); Total eclipses (1704); Spectrometers (1554); Solar E corona (1990)

1. Introduction

Observations of infrared (IR) solar coronal emission lines are currently of significant interest, motivated by the need to directly measure coronal magnetic fields (Judge et al. 2001; Penn 2014) and by the advent of new instrumentation, especially the Daniel K. Inouye Solar Telescope (DKIST; Tritschler et al. 2016; Rimmele et al. 2020). Many IR lines are strongly photoexcited and are therefore promising for accurately measuring Doppler shifts and nonthermal line widths at significant heights above the limb (Del Zanna & DeLuca 2018). In addition, observations of these lines are needed to inform the design of new instrumentation for coronal magnetometry.

In their coronal magnetometry feasibility study, Judge et al. (2001) find that the two most promising methods for observing the coronal magnetic field are measuring the Zeeman and Hanle effects in polarized emission lines. The Zeeman effect modulates the circular polarization and provides a means of measuring the line-of-sight (LOS) field magnitude, while the Hanle effect is encoded in the linear polarization and gives a measurement of the plane-of-sky field direction (Casini & Judge 1999; Lin & Casini 2000; Judge et al. 2001). For sufficient sensitivity, circular polarization measurements require emission lines at visible or IR wavelengths. Magnetically induced Zeeman splitting varies with wavelength as λ^2, while thermal broadening goes as λ. In addition, the effects of instrumental and atmospheric scattering are less significant at longer wavelengths.

In the visible and infrared, strong coronal emission lines are formed by forbidden magnetic dipole (M1) transitions. A modeled spectrum (a reproduction of Figure 2 from Judge 1998) is shown in Figure 1. Historically, the corona has been observed infrequently above 1 μm (Del Zanna & DeLuca 2018), and these lines are not as well understood as their visible and near-IR counterparts. Exploration of this wavelength region has become more affordable with the availability of high-sensitivity, large-format, commercial off-the-shelf (COTS) detectors.

Based on the modeled intensities in Figure 1, Judge et al. (2001) list the most promising candidates for magnetic field measurements (reproduced in Table 1). The lines near the center of the table are good candidates for making magnetic field measurements because they balance the short-wavelength advantages of high line intensity and low thermal emission with the long-wavelength benefits of high sensitivity to magnetic field and low scattered light. However, these candidate lines must be characterized before spectropolarimeters can be designed around the most useful ones. At the time of the 2017 total solar eclipse, five of the promising lines in Table 1 had never been observed: Si IX 2.584 μm, Fe IX 2.855 μm, and the three lines with $\lambda > 5$ μm (Del Zanna & DeLuca 2018). Most of the IR lines that had been measured were not well characterized spatially or temporally (e.g., Olsen et al. 1971; Kuhn et al. 1996; Judge et al. 2002).

This paper describes the Airborne Infrared Spectrometer (AIR-Spec), a new instrument that was developed to identify and characterize magnetically sensitive infrared coronal lines and assess their suitability for future ground-based, airborne, and space-based spectropolarimetric observation. The lines targeted for observation are highlighted in Figure 1 and Table 1. Section 2 describes the science goals and the instrument design, implementation, and deployment. Section 3 summarizes the observations, details the data processing and calibration schemes, describes the available data, and summarizes the lessons learned.

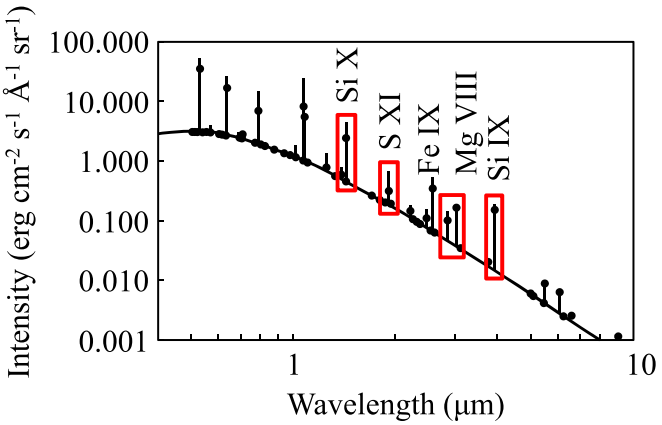

Figure 1. Predicted spectrum of M1 lines at 1.1 $R_\odot$ (Judge 1998). Black circles are intensity values for collisional de-excitation only; straight lines include radiative contributions. The smooth baseline is the coronal continuum produced by Thomson scattering by free electrons. Lines outlined in red were measured by AIR-Spec during the 2017 eclipse.

Table 1
Candidate M1 Lines for Coronal Magnetic Field Measurements (Judge et al. 2001)

Ion	λ (μm)	log T_e (K)	F_E	$F_{\rm scat}$ (photons cm^{-2} s^{-1})	$F_{\rm th}$	T (%)
Fe XIV	0.530	6.30	$2.57+8$	$2.78+8$	8.22–32	100
Fe X	0.637	6.03	$1.77+8$	$1.37+8$	3.96–24	100
Fe XI	0.789	6.10	$1.48+8$	$5.48+7$	7.21–17	100
Fe XIII	1.075	6.22	$4.91+8$	$1.26+7$	7.27–9	100
Si X	**1.430**	**6.13**	$\mathbf{1.57+8}$	$\mathbf{2.88+6}$	**1.85–3**	**50**
S XI	**1.920**	**6.25**	$\mathbf{3.59+7}$	$\mathbf{5.85+5}$	$\mathbf{2.21+1}$	**50**
Si IX	2.584	6.04	$6.07+7$	$1.11+5$	$2.01+4$	0
Fe IX	**2.855**	**5.94**	$\mathbf{1.60+7}$	$\mathbf{6.31+4}$	$\mathbf{1.23+5}$	**60**
Mg VIII	**3.027**	**5.92**	$\mathbf{2.73+7}$	$\mathbf{4.51+4}$	$\mathbf{3.27+5}$	**100**
Si IX	**3.935**	**6.04**	$\mathbf{5.67+7}$	$\mathbf{1.01+4}$	$\mathbf{1.17+7}$	**60**
Mg VII	5.502	5.80	$3.20+6$	$1.42+3$	$2.80+8$	10
Fe XI	6.081	6.10	$2.61+6$	$7.88+2$	$5.62+8$	50
Mg VII	9.031	5.80	$9.53+5$	$7.66+1$	$3.79+9$	90

Note. From left to right, the columns list the ion, transition wavelength, formation temperature in ionization equilibrium, emission-line flux, scattered light, thermal emission, and atmospheric transmission at 8 km. The boldface rows correspond to transitions measured by AIR-Spec during the 2017 eclipse.

2. The Airborne Infrared Spectrometer

AIR-Spec is a slit spectrometer that was designed to search for infrared emission lines of Si X, S XI, Fe IX, Mg VIII, and Si IX in the solar corona during the total solar eclipse on 2017 August 21. AIR-Spec was funded by a Major Research Instrumentation grant from the National Science Foundation (NSF) with cost-sharing by the Smithsonian Institution. It observed the eclipse from the NSF/NCAR Gulfstream V High-performance Instrumented Airborne Platform for Environmental Research (GV HIAPER).

2.1. Goals and Specifications

The upper half of Table 2 lists the predicted rest wavelengths, intensities, and line widths of the five AIR-Spec lines. In addition to identifying its target lines, AIR-Spec was designed to characterize line emission as a function of solar conditions and radius, providing information on the radiative excitation of each line (Habbal et al. 2011), and to search for time-varying Doppler velocities in the lines, including high-frequency velocity oscillations, which are thought to be the signatures of waves or flows (Tomczyk et al. 2007; Pontieu & McIntosh 2010). The instrument performance, shown in the lower half of Table 2, is sufficient to address these goals.

The spectral range extends from each predicted central wavelength ± 200 Å, allowing for the 0.1% wavelength uncertainty (Judge 1998) plus a 500% margin. The spectral resolution broadens each line by only a factor of 2–3. The spectral dispersion provides 5–6 pixels across each measured FWHM, allowing centroid performance to be determined by signal-to-noise ratio (S/N) alone. The 1.55 $R_\odot$ field of view (FOV) is sufficient to sample different coronal conditions with a single slit position, while the 11″–13″ spatial resolution is sufficient to distinguish between different coronal features. Near the limb where the corona is brightest, a 30 s exposure provides S/N sufficient to detect all of the lines and a 1 s exposure provides 5 km s^{-1} velocity resolution on Si X.

The instrument performance in Table 2 was achieved by imposing requirements on the optical design, the precision of the optical alignment, the surface quality and efficiency of each optic, the image stability over each exposure, and the thermal design of the camera and spectrometer. The optical design (Section 2.2.1) provides the specified spectral range, spectral dispersion, spatial FOV, and spatial sampling. Achieving the spectral and spatial resolution requires rms mirror surface figure errors below 1/20 of a (633 nm) wave, alignment tolerances on the order of 20 μm and 40″ (Section 2.3), and an rms image stability of 2 pixels or 4.″6 (Section 2.2.2). The S/N performance was obtained by purchasing mirrors and optical windows with high (85%–98%) optical efficiencies, cooling the spectrometer to 150 K (Section 2.2.3), and purchasing an IR camera with high quantum efficiency (QE), low dark current and read noise, and a front end designed to minimize thermal emission (Sections 2.2.1 and 2.2.3).

2.2. Design and Implementation

AIR-Spec consists of an image stabilization system, telescope, infrared spectrometer, and visible slit-jaw imager (Figure 2). The image stabilization system keeps the Sun fixed in the telescope FOV as the airplane moves. The telescope focuses onto a mirrored slit-jaw, where the light is divided into two channels. Visible light reflected by the slit-jaw is imaged by a slit-jaw camera, while infrared light passing through the slit is dispersed by a diffraction grating and focused onto an infrared detector. The telescope entrance pupil is imaged onto the diffraction grating in a collimated beam.

The telescope and spectrometer were designed in Zemax and implemented using a mixture of custom and modified COTS components, as detailed in Section 2.2.1. Alignment sensitivities for each individual optic were determined using Zemax, and an error budget was compiled in order to define the requirements on alignment, optical surface quality, and image stability. In lieu of a full stray light analysis (e.g., using nonsequential Zemax or FRED), the cryostat design (Section 2.2.3) was informed by hand calculations that estimated the photons scattered and emitted onto the detector from various sources inside the spectrometer.

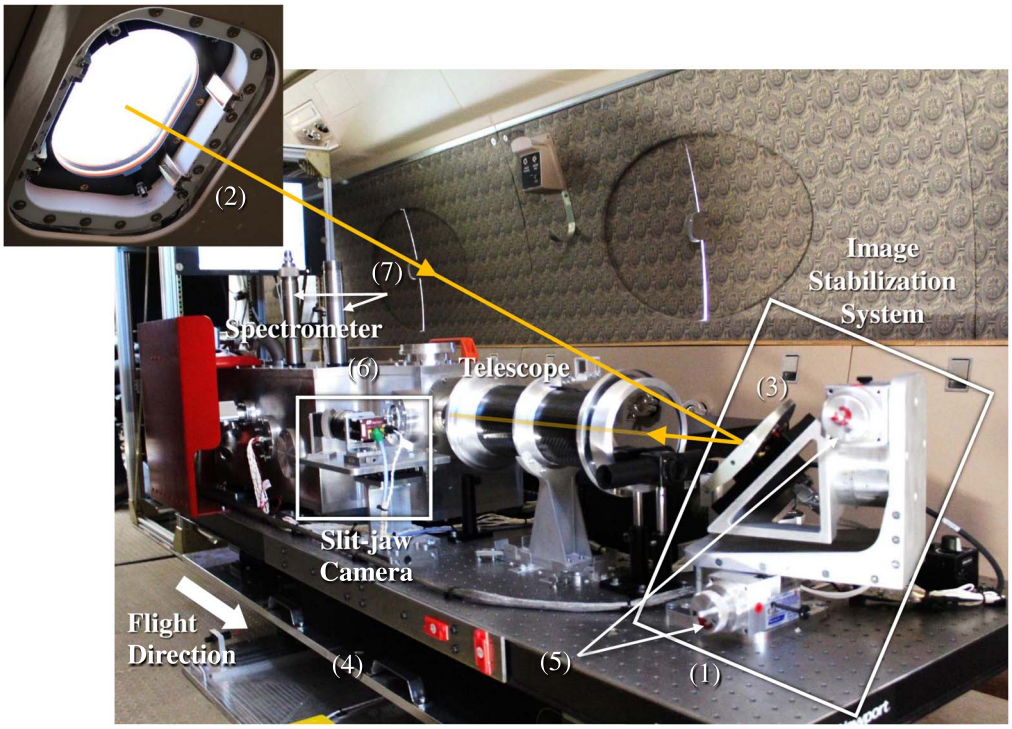

Figure 2. AIR-Spec on board GV HIAPER. The instrument is installed on the floor on the port side of the cabin toward the front of the plane. The image stabilization system, telescope, spectrometer, and slit-jaw camera are mounted on a vibration-isolated optical bench (1). Light enters through a small viewport (2) on the upper starboard side of the fuselage and is reflected into the telescope by a fast-steering mirror (3). The optical bench is translated fore–aft and left–right (4) and the mirror rotated about two axes (5) to facilitate alignment of the Sun, window, mirror, and telescope. The spectrometer optics are contained in a vacuum chamber (6) and cooled with liquid nitrogen (7).

Table 2
Predicted Emission-line Properties and Measured Instrument Performance

	Si X	S XI	Fe IX	Mg VIII	Si IX
Rest wavelength[a] (μm)	1.43	1.92	2.86	3.03	3.93
Thermal line width[b] (Å)	2.3	3.1	4.6	4.9	6.3
Intensity[c] at 1.1 $R_\odot$	39	8.8	4.0	6.7	13
(10^{11} photons s^{-1} cm^{-2} sr^{-1})	55	5.1	7.2	14	12
Spectral range (μm)	1.42–1.54	1.87–1.99	2.83–3.07	2.83–3.07	3.75–3.98
Spectral dispersion (Å $pixel^{-1}$)	1.19	1.17	2.37	2.37	2.33
Spatial FOV ($R_\odot$)	1.55	1.55	1.55	1.55	1.55
Spatial sampling (arcsec $pixel^{-1}$)	2.31	2.31	2.31	2.31	2.31
Spectral resolution (Å)	7.5	7.5	15	15	15
Spatial resolution (arcsec)	11	13	11	11	13
S/N[d] of line center	140	10	7	7	12

Notes.
[a] Rest wavelengths were predicted by Judge (1998).
[b] Thermal line widths were extrapolated from measurements of the 530.3 nm Fe XIV (Contesse et al. 2004).
[c] Original intensities (top row) were predicted by Judge (1998). Updated atomic data were used in new intensity estimates (bottom row) by Del Zanna & DeLuca (2018).
[d] S/N is specified for a 30 s exposure over 35″ at the limb.

2.2.1. Optical System

Figure 3 shows a ray-trace of the AIR-Spec telescope and spectrometer. Light is collected by the $f/15$ Cassegrain telescope (10 cm primary, 1.5 m focal length) and focused onto a 70 μm (9.″6) entrance slit. The slit is cut into an aluminum coating on a 2 mm thick sapphire substrate. The aluminum coating is on the front surface of the substrate and reflects light into a slit-jaw camera. Stray reflections from the uncoated back surface introduced spectral artifacts in the 2017 data that were misinterpreted as emission lines (Samra et al. 2019). A backside metal shield was later added to absorb these reflections, as described in Section 4.

The light exiting the slit is collimated by a 0.7 m focal length spherical mirror, and the collimated light is incident on a reflective planar diffraction grating with 10 μm groove spacing. The grating is a replica on a Pyrex substrate that was custom

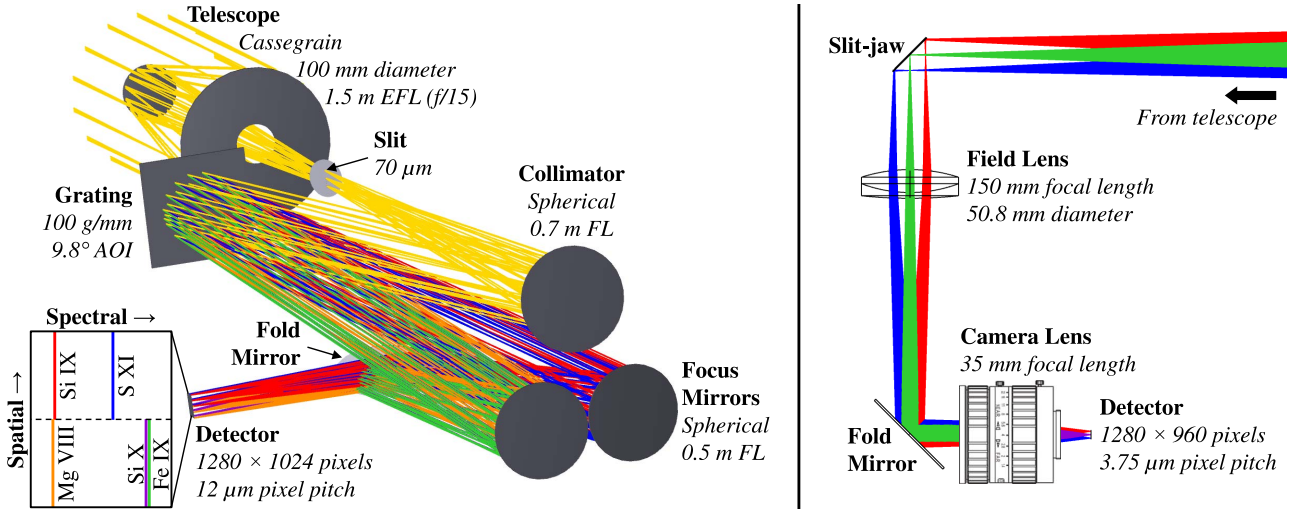

Figure 3. Left: ray-trace of the AIR-Spec telescope and spectrometer, including the layout of emission lines on the infrared detector. Different ray colors indicate different wavelengths. Right: ray-trace of the slit-jaw camera optics. Different ray colors indicate different field angles.

made by Thorlabs. It has 10 μm groove spacing, a blaze angle of 9°.7, an aluminum coating, and an efficiency that ranges from 23% to 79% at the five wavelengths of interest. The grating is used in a near-Littrow configuration, so that the diffracted wavelengths are nearly coincident with the incoming light. The five wavelengths of interest are diffracted into two groups: second-order 1.92 μm rays near first-order 3.93 μm rays, and second-order 1.43 μm rays near first-order 2.86 and 3.03 μm rays. Two 0.5 m focal length spherical mirrors focus the two wavelength groups onto the top and bottom of the detector. The 3 and 4 μm channels include second-order light at 1.5 and 2 μm, respectively. The detector layout is shown in Figure 3. The spectral and spatial characteristics of each channel are listed in Table 2.

Custom optics were purchased for the telescope primary and secondary, the spectrometer collimator and focus mirrors, and the diffraction grating. The spectrometer fold mirror is an off-the-shelf part that was cut to size after purchase, and the slit-jaw substrate is an off-the-shelf sapphire window with a custom coating.

The infrared camera is an IRC912 from IRCameras (https://ircameras.com) with a custom focal plane (Lockheed Martin Santa Barbara Focalplane model SBF204), multiband cold filter, cold stop, and antireflection-coated Dewar window. This was the only camera within our budget that met our requirements for sensitivity, noise, resolution, and format. Its specifications are summarized in Table 3.

The SBF204 readout integrated circuit, with 50,000 electron well depth and <32 electron read noise, is specifically designed for low photon flux applications. The average quantum efficiency of the InSb sensor is >90% due to its wideband 1–5.3 μm antireflection coating. The cold filter and cold stop, both operating at 59 K, shield the focal plane from thermal photons outside the FOV and/or passband. The focal plane itself also runs at 59 K, reducing the dark current to about 65,000 $e^- s^{-1}$ $pixel^{-1}$.

The focal plane has 1024 pixels along the spectral dimension and 1280 pixels along the spatial dimension (640 pixels per channel). The 12 μm pixel pitch provides a linear dispersion of about 2.4 Å $pixel^{-1}$ in first order (1.2 Å $pixel^{-1}$ in second order) and a plate scale of 2.″3 $pixel^{-1}$. The spectral width of each channel is about 2400 Å in first order and 1200 Å in second order. The slit length is 0°.4 (1.5 $R_\odot$). During the eclipse, the IR camera operated at a cadence of 15 frames s^{-1}. Most of the coronal data were collected with a 60 ms exposure time.

Table 3
Characteristics of the Infrared Camera

Material	InSb
Wavelength range	1.0–5.3 μm
Operating temperature	59 K
Format	1280 × 1024 pixels
Pixel pitch	12 μm
Well depth	50,000 e^-
Quantum efficiency	> 90%
ADC gain	3.25 e^-/DN
Readout noise	< 32 e^-
Dark current	65,000 $e^- s^{-1}$ $pixel^{-1}$

The IR detector has high spatial uniformity, as judged from flat-field data taken by the manufacturer at 2 ms exposure time. (It was not possible to introduce a Lambertian source into the cold cryostat in order to repeat this test at a more representative exposure time.) The first two panels in Figure 4 show the spatial variation of the two-point nonuniformity correction across the detector. A total of 98% of pixels have an offset between −300 and 300 DN and a gain between 0.95 and 1.05 DN/DN. Local variations in the gain are much smaller, as seen in the third panel. The gain standard deviation is less than 0.02 DN/DN in 99% of 9 × 9 pixel neighborhoods.

The white-light slit-jaw camera provides context imagery for the infrared spectra. Light from the mirrored slit-jaw is reimaged by a monochrome visible camera, in which the slit appears as a dark line superimposed on the corona. Both the white-light camera and its lens are commercially available products. They were chosen to match or exceed the FOV, spatial resolution, and cadence of the spectrometer and to make software integration as simple as possible. The camera is a Prosilica GC1290 from Allied Vision Technologies, with 1280 × 960 3.75 μm pixels. It has a gigabit Ethernet interface, a global shutter, a maximum frame rate of 33 Hz, a quantum efficiency of 30%–60% at visible wavelengths, and a 12-bit ADC. The f/1.4, 35 mm camera lens is a Fujinon CF35HA-1. A field lens ensures that the off-axis rays from the slit-jaw are

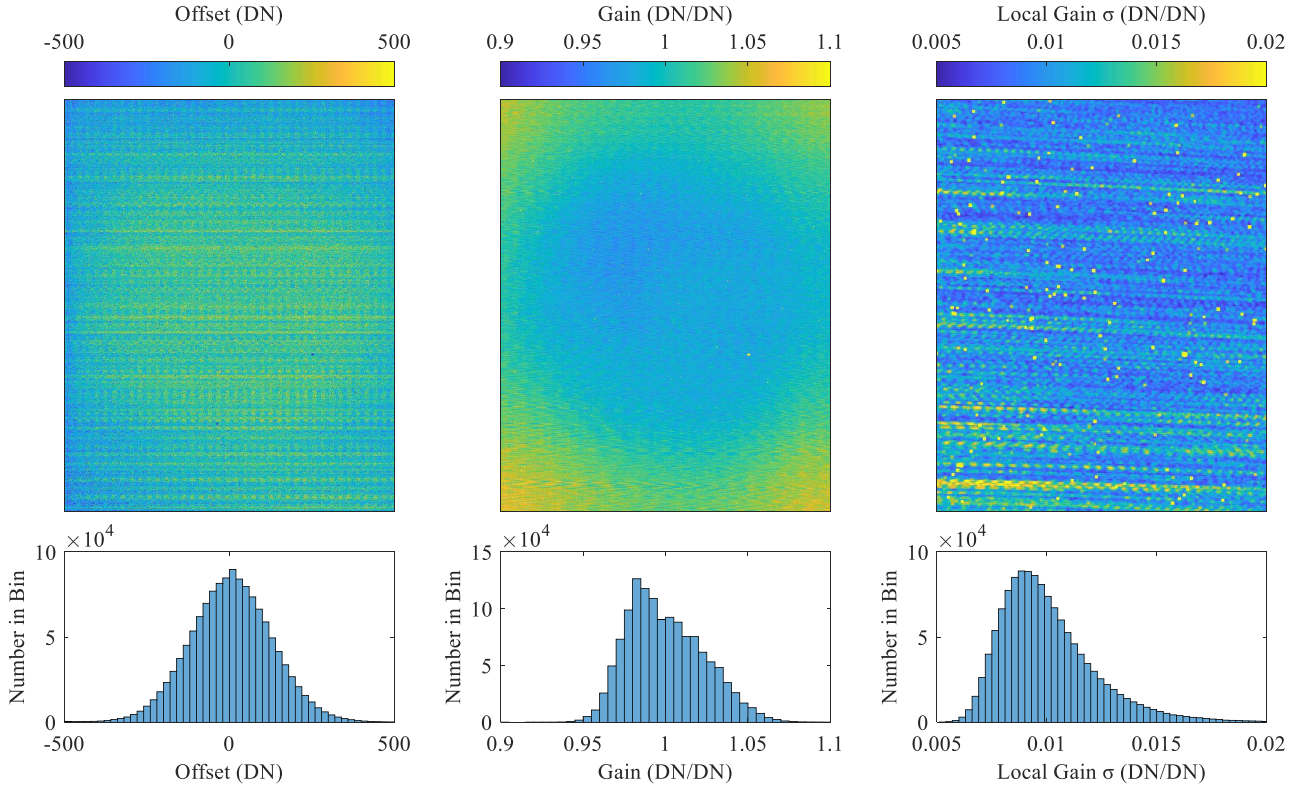

Figure 4. Maps and histograms of spatial nonuniformity across the detector. The left and middle panels show the offset and gain needed to perform a two-point nonuniformity correction at every pixel. The right panel shows the gain standard deviation in each local 9 × 9 pixel neighborhood.

not vignetted at the camera lens. The field lens is a 150 mm achromat that serves as the vacuum chamber exit window for the light reflected from the slit-jaw. The lens-camera system has a plate scale of $2\farcs3$ pixel^{-1} (equivalent to the IR camera plate scale), a 2.3 $R_\odot$ FOV (1.5 times larger than the IR camera FOV), and a cadence of 33 frames s^{-1} (about twice the IR camera cadence). During totality, the exposure time was set to 1 ms to provide a well-exposed inner corona. A ray-trace of the slit-jaw camera optics is shown in Figure 3.

The two main challenges of implementing the AIR-Spec optical design were (1) pointing the telescope at the Sun stably and continuously and (2) minimizing the level of the dark instrument background. Pointing and stabilization were achieved by actively controlling the LOS with a fast-steering mirror and manually adjusting the mirror and table to compensate for changes in viewing geometry. The instrument background was reduced by cooling the spectrometer optics and infrared camera. Figure 2 shows AIR-Spec installed in the GV cabin with image stabilization and cooling system components identified.

2.2.2. Pointing and Image Stabilization

During the 2017 eclipse, AIR-Spec observed through a 150 × 220 mm double-paned sapphire viewport on the upper starboard side of the aircraft cabin. Sapphire was chosen because it provided high transmission (around 85% per windowpane) from visible to mid-IR wavelengths. To minimize its birefringence, the sapphire was cut with its fast axis normal to the plane of the window. For cost and schedule reasons, the sapphire panes were designed to conform to a standard GV viewport that was already certified to fly. This required that all four semireflective surfaces be parallel, resulting in an etalon effect that produced fringes in one of the spectrometer channels (see Section 3.2.5).

The instrument was mounted to the floor on the port side of the cabin, where a fast-steering mirror on the optical bench directed sunlight from the window into the telescope (Figure 2). Since both the FOV through the window and the mirror range of travel were limited, the instrument was positioned fore–aft and left–right using linear sliders and the mirror normal was aligned using two manual rotary adjusters on its mount. A custom alignment tool similar to a telescope reflex sight was used to place the Sun in the telescope through the window as the instrument was translated and the mirror was rotated. The alignment tool superimposed an LED referencing the telescope LOS onto a view of the Sun through the aircraft window.

Image stability was addressed in two ways. First, the optical bench was isolated from the effects of high-frequency airframe vibration by six tuned isolators placed between it and the aircraft floor. Second, the remaining low-frequency perturbations were compensated by a closed-loop fast-steering mirror that fed a stabilized beam into the telescope. The mirror was dynamically positioned so that the LOS from the Sun was normally incident on the telescope. The image stabilization requirement was $4\farcs6$ (2 pixels) rms over each 60 ms camera exposure. During the 4-minute eclipse observation, 92% of exposures achieved this requirement (Figure 5).

The image stabilization is shown schematically in Figure 5. Computations are performed at 500 Hz by a real-time computer. The mirror command is calculated from three inputs: the eclipse ephemeris (computed using GPS location and time), aircraft attitude given by the integrated gyroscope rates, and slit position coordinates from the operator. In order to

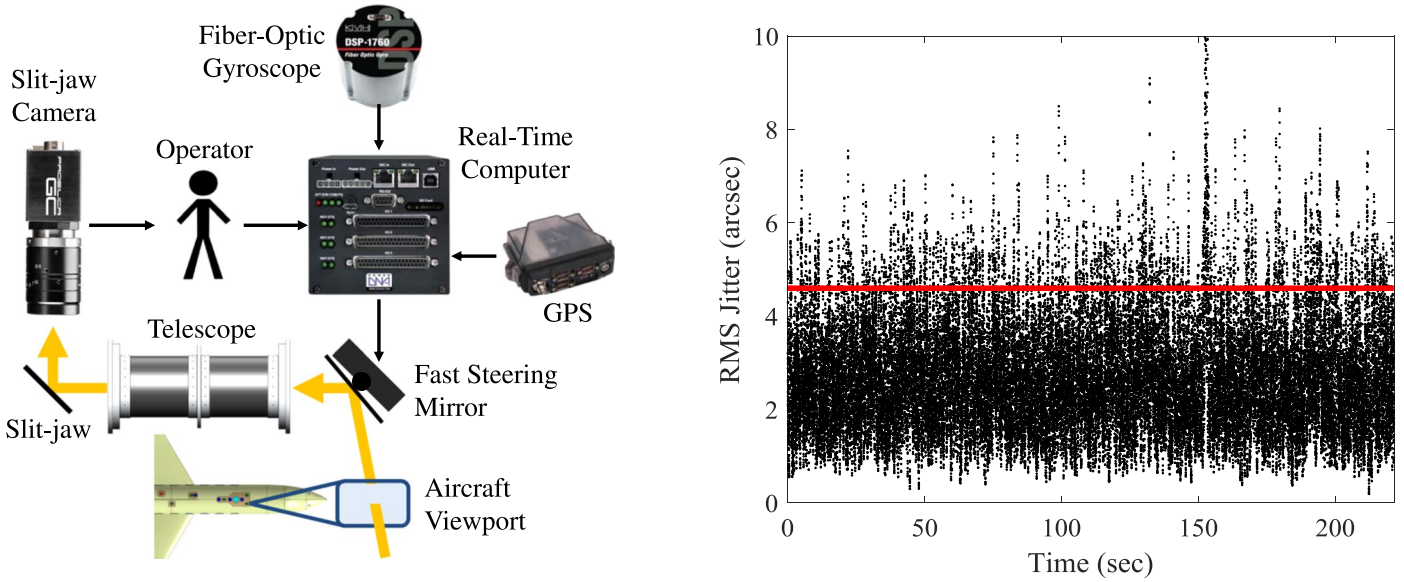

Figure 5. Image stabilization system block diagram (left) and performance (right). The rms jitter for each 60 ms exposure is plotted in black. The 2-pixel Nyquist limit is the red line. A total of 92% of exposures have jitter below the Nyquist limit.

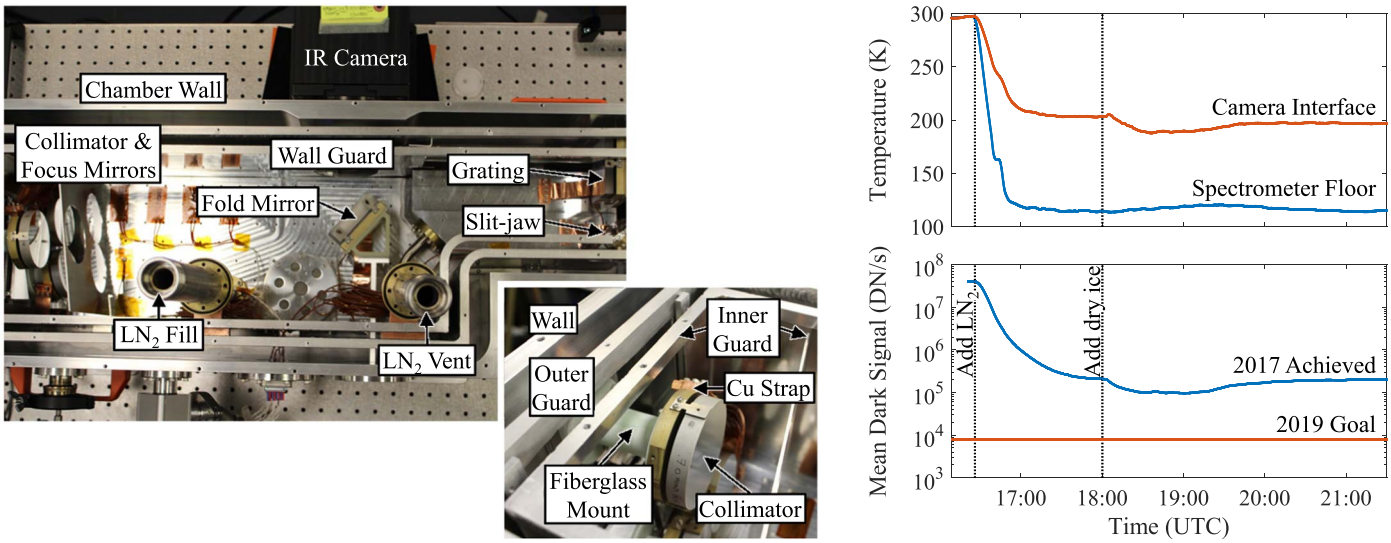

Figure 6. Thermal background reduction. Left: top-down view of the AIR-Spec vacuum chamber before it was blackened to reduce stray light. The spectrometer optics and IR camera are labeled. Liquid nitrogen enters through the LN_2 fill port, and nitrogen gas is released through the vent. Copper straps connect the optics to the floor, which is the top of the liquid nitrogen Dewar. Inset: detail of the collimator mount and cooling strap. To maximize stability, each optic is mounted to the warm chamber wall with G10, a thermally isolating fiberglass composite. A thermally conducting copper strap attaches the optic to the cold spectrometer floor. Inner and outer wall guards block radiation from the warm chamber wall. Right: effect of cooling the instrument.

position the slit, the operator monitors a video of the white-light corona from the slit-jaw camera.

2.2.3. Thermal Background Reduction

Because of their close proximity to the focal plane, the slit-jaw, collimator, grating, focus mirrors, and camera fold mirror emit enough radiation at room temperature to overwhelm the coronal signatures. Radiation from the slit-jaw is especially significant because it is imaged onto the focal plane by design. In order to maximize S/N, the slit-jaw and all subsequent optics are cooled to 150 K. To achieve this while keeping the optics dry and stable, the entire spectrometer is housed in a vacuum chamber at a pressure below 10^{-3} torr. The chamber floor is the top of a liquid nitrogen Dewar, which serves as the heat sink for the components inside the chamber. The 2 L Dewar has a hold time of over 1 hr once the system reaches thermal equilibrium.

Inside the vacuum chamber, the optics are mounted to thermally isolated tungsten temperature-spreader plates and attached with copper straps to the floor. Tungsten was chosen for its combination of high thermal conductance (164 W m^{-1} K^{-1}) and low coefficient of thermal expansion (CTE, 4.4 ppm/°C). Wall guards chilled to <150 K shield the detector from thermal radiation from the warm walls, and the wall guards and floor are blackened to reduce reflectivity. Figure 6 shows the inside of the vacuum chamber, including the spectrometer optics, liquid nitrogen ports, and chilled wall guards. Two feedthrough micrometers on the focus mirrors (not shown) allow cold alignment of the two channels on the

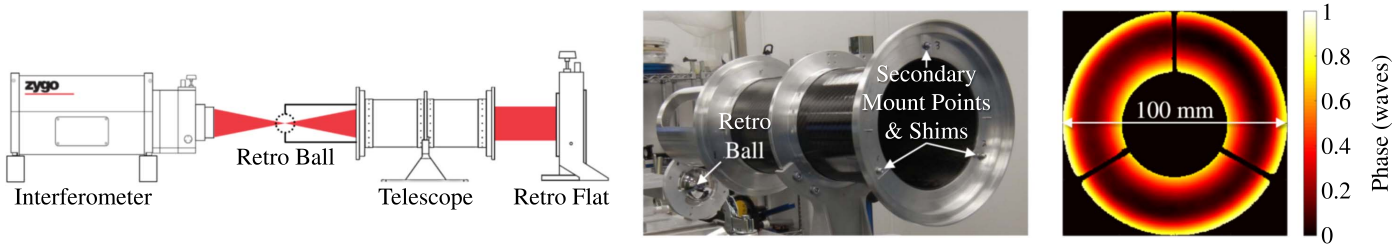

Figure 7. Telescope alignment. Left: optical setup, including the Zygo interferometer, retro ball, AIR-Spec telescope, and retro flat (Zygo Corporation 2015). Middle: aligning the secondary mirror. The retro ball is off-axis, allowing the Zygo laser beam to pass through the system. The secondary is tilted and focused by shimming with washers at the three points indicated. Right: double-pass wave front for the final telescope alignment, after zeroing tip and tilt. The phase variations are due to a combination of defocus and the $\lambda/20$ rms surfaces of the primary and secondary.

detector. The inset shows in more detail how the optics are mounted and cooled.

The infrared camera includes several features to help minimize its dark background. As described in Section 2.2.1, the focal plane was chilled to 59 K by a closed-cycle cooler in order to reduce the dark current to 65,000 $e^- s^{-1}$ $pixel^{-1}$. The thermal background was reduced by a cold stop, which limited the FOV, and a cold bandpass filter, which removed light outside the instrument passbands.

In spite of these features, we observed significant thermal emission originating from the front end of the camera. This was a much larger contributor to the dark background than either dark current or thermal emission from inside the spectrometer. We created a thermal model of the camera housing and the nearby wall of the spectrometer, compared the modeled results to thermocouple measurements, and determined that heat from the camera cryocooler was conducting into the front of the camera housing and emitting onto the detector. We reduced thermal emission from the housing in two ways: we packed the camera−spectrometer interface in dry ice, and we placed a cold baffle assembly in contact with the camera entrance window. The aluminum/copper baffle attaches directly to the cold inner wall guard and uses thermally conductive gasketing material to make a thermal connection to the camera window.

Chilling the spectrometer with liquid nitrogen and the camera housing with dry ice reduced the thermal background by a factor of 400 compared to room-temperature operation (Figure 6). During the 2017 eclipse, the background level was on the order of 10^5 DN s^{-1}, and a 60 ms exposure time limited the background to half the 15,000 DN well depth. Ahead of the 2019 eclipse, IRCameras completed a redesign and rebuild of the camera that reduced the background by an additional factor of 30. Section 4 describes the camera modifications needed to achieve this improvement.

2.3. Optical Alignment

The AIR-Spec alignment took place in five steps. First, the telescope secondary was aligned to the primary. The internal spectrometer optics were aligned next, and then the slit-jaw camera was aligned to the slit-jaw. Finally, the telescope was aligned and focused relative to the spectrometer, and the image stabilization components were aligned to the telescope.

The purpose of the optical alignment was to minimize the instrument point-spread function (PSF) and center and focus the image on each camera. Because small misalignments could be compensated by adjusting focus, it was sufficient to align each optic to several hundred microns in centration and several arcminutes in tilt. With the system aligned to this level, misalignment had a negligible effect on PSF compared to imperfections in the mirror surfaces.

2.3.1. Telescope Alignment

The method for aligning the AIR-Spec telescope was modeled on the alignment procedure for the Atmospheric Imaging Assembly (AIA) telescopes (Lemen et al. 2012; W. Podgorski private communication to V. Marquez 2017). Before the primary and secondary mirrors were aligned, a corner cube was positioned to reference the mechanical boresight of the telescope tube. Two crosshair reticles were mounted at either end of the tube, one in the primary mirror hole and the other in place of the secondary. An alignment telescope was used to find the line through both reticles, and this line was defined as the mechanical boresight. With the alignment telescope in auto-collimation mode, a retro-reflecting flat mirror was aligned to both telescopes. Finally, the corner cube was aligned to the retro flat using a theodolite and bonded into place.

The secondary mirror was aligned to the primary with the telescope in the double-pass configuration shown in Figure 7 (left), from a Zygo application note on typical interferometer setups (Zygo Corporation 2015). A Zygo interferometer (model GPI-4-XP 512, 633 nm wavelength) fed the telescope and precisely measured the tip, tilt, and defocus of the returned wave front, which was reflected back through the system by the retro flat. The focal point was defined by the center of a removable retro-reflecting ball mounted to the back of the telescope.

The interferometer was outfitted with an $f/7.2$ Dynaflect transmission sphere, suitable for aligning reflective surfaces, and the focus of the spherical beam was placed at the nominal telescope focus by translating the interferometer until the wave front was approximately flat. The final wave front had a peak-to-valley height of 0.76 waves and a power term of 0.13 waves, corresponding to about 3 μm lateral displacement and 30 μm axial displacement of the focal point from the center of the retro ball.

Next, the retro ball assembly was removed from the rear telescope flange and mounted upside down, maintaining the tilt of the telescope while allowing the interferometer beam to pass through it (Figure 7, center). The secondary mirror was shimmed with washers at its three mounting points, resulting in a final tilt of 28 waves (270 μm lateral displacement) and defocus of 0.23 waves (260 μm axial displacement). The right plot in Figure 7 shows the double-pass wave front after zeroing tip and tilt by adjusting the retro flat. In addition to defocus, the variations across the wave front come from imperfections in the mirror surfaces.

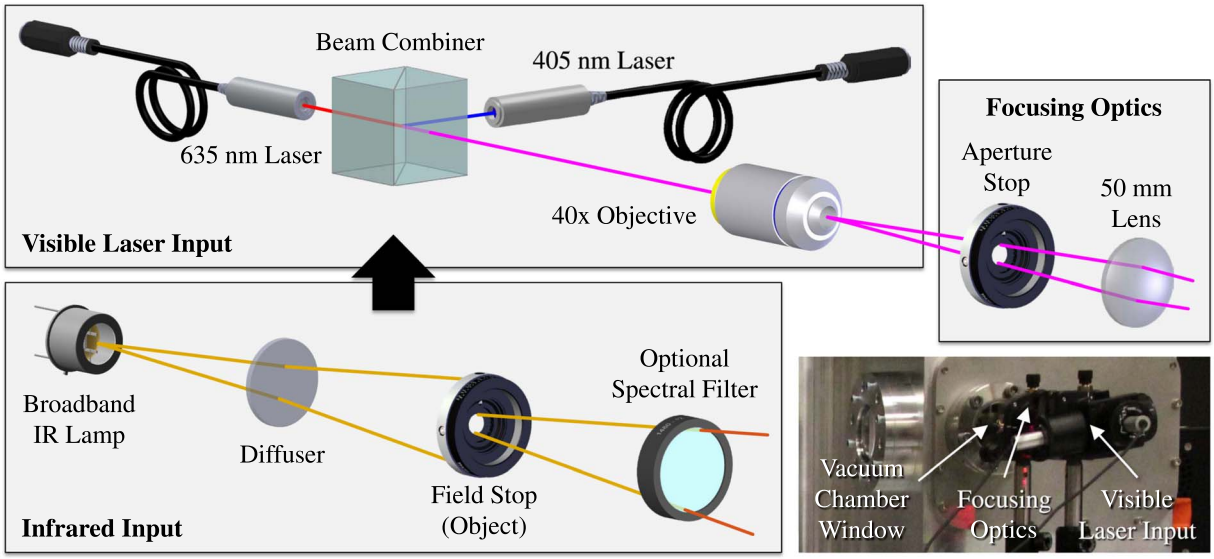

Figure 8. Input options for spectrometer alignment. The focusing optics are fed by either two visible lasers or a broadband IR lamp. The focusing optics image the object (microscope objective spot or IR-illuminated field stop) onto the slit through the vacuum chamber window (bottom right).

2.3.2. Spectrometer Alignment

The spectrometer alignment was complicated by the number of optical elements and the nonaxial light path. However, the long depth of focus (0.5 mm) and the use of spherical mirrors provided relatively loose alignment tolerances that were achieved using shims and measurement tools such as a shear plate, a ruler, and the IR camera. Because all of the spectrometer optics were either planar or spherical, decenter could be compensated by tilt with little effect on PSF. Therefore, it was sufficient to center the light path on each optic to about 0.5 mm and precisely align the image on the detector by tilting the focus mirrors with a set of micrometers.

Two input assemblies were constructed to allow alignment in both visible and infrared light (Figure 8). The visible laser assembly combined red (635 nm) and blue (405 nm) lasers with a 50–50 beamsplitter. A 40× microscope objective was used to create a fast divergent beam. The infrared assembly consisted of a field stop (iris aperture) illuminated by a diffuse broadband IR source. One of several exchangeable filters could be included to tailor the spectral output. A 50 mm MgF_2 lens focused light from the operational assembly, imaging the object (microscope objective spot or IR-illuminated field stop) onto the spectrometer slit-jaw. The lens was placed approximately 75 mm from the object and 150 mm from the slit, providing a magnification of about 2. The *f* number was set by another iris, which acted as an aperture stop. The spectrometer was aligned according to the following procedure:

1. A 50 μm pinhole was mounted in place of the slit-jaw. The laser input assembly (with the blue laser off) was aligned through the pinhole to the center of the collimating mirror, defining the optic axis.
2. *Pinhole focus:* A shear plate was used to check the beam from the collimating mirror. The mirror was shimmed until the shear plate fringes were parallel to the fiducial line, indicating that the pinhole was coincident with the mirror focal point (Figure 9(a)).
3. *Collimator tilt:* The 50 μm pinhole was replaced by a 400 μm pinhole, and the blue laser was turned on. The collimating mirror was tilted about two axes until the beam was centered on the diffraction grating (Figure 9(b)).
4. *Grating tilt:* The grating was tilted about two axes until the sixth-order beam from the red laser ($m\lambda = 3.810$ μm) and the seventh-order beam from the blue laser ($m\lambda = 2.835$ μm) landed in their intended locations on the two focus mirrors (Figure 9(c)).
5. The laser assembly was replaced by the IR assembly. The field stop was adjusted to fully illuminate the pinhole while underfilling the 25 mm pinhole substrate, to prevent stray light from reaching the detector. The illuminated pinhole produced a bright line in each channel of the IR camera.
6. *Focus mirror tilt:* Narrowband filters centered at 1480 and 1900 nm were added one at a time. Using the feedthrough micrometers (Figure 9(d)), each focus mirror was tilted about two axes until the line was centered vertically in the channel and the spectral passband was centered at the intended horizontal pixel (Figure 9(e)).
7. *Grating rotation:* The narrowband filters were removed. The grating was rotated in-plane until the line in each channel was approximately horizontal (Figure 9(f)).
8. *Camera focus:* The 400 μm pinhole was replaced by the 50 μm pinhole (an approximate point source). The focus of the pinhole image was checked in both channels. The PSF was about as wide as predicted, so the focus mirrors were not moved.
9. *Slit rotation:* The 400 μm pinhole was removed, and the slit-jaw was mounted in its place. The field stop was adjusted to overfill the slit while underfilling the slit-jaw. The slit-jaw was rotated in-plane until the observed atmospheric absorption features were approximately vertical in both channels (Figure 9(g)). Although the alignment was performed indoors, the absorption was measurable owing to the long path length in the open vacuum chamber.
10. *Slit focus:* The top and bottom edges of the slit image were checked in the IR camera. The top edge was well focused, indicating that the slit-jaw did not need to be adjusted. Light from the bottom of the slit was vignetted by the slit-jaw

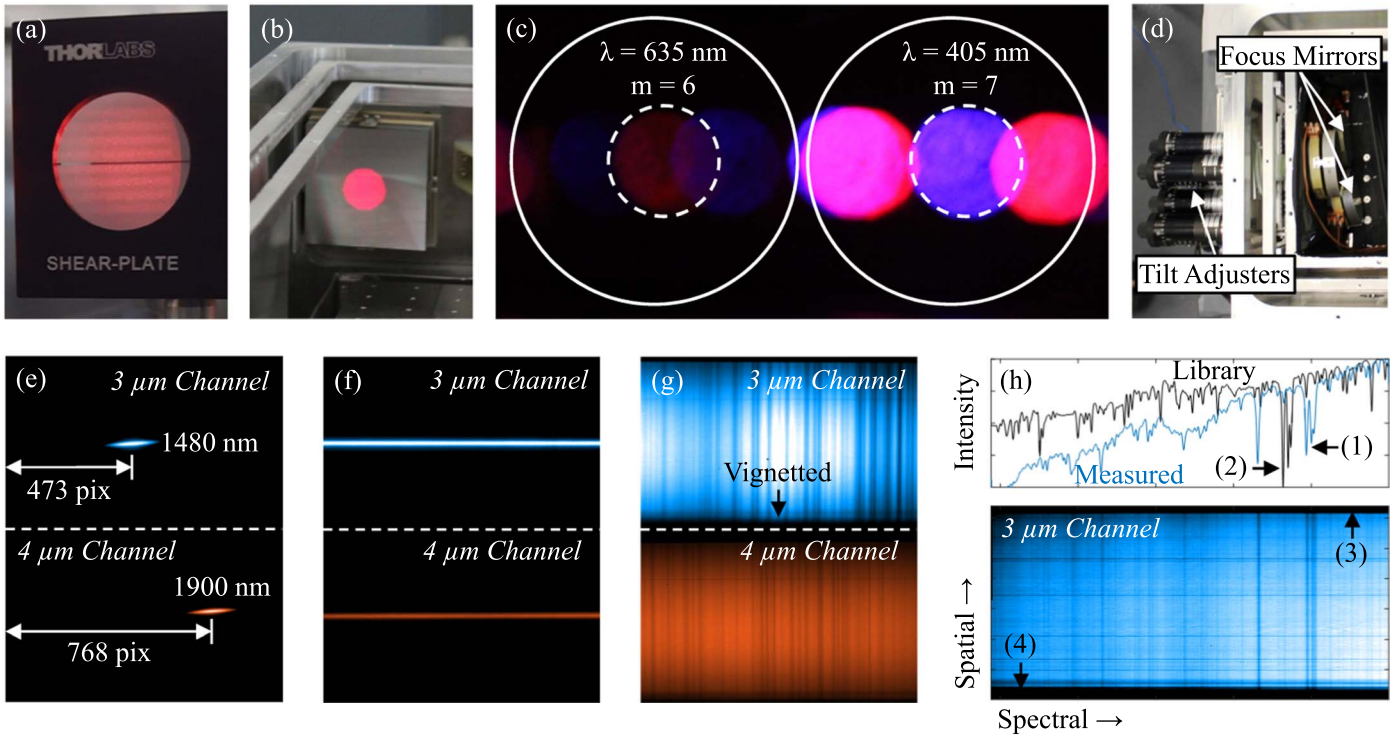

Figure 9. Alignment of the spectrometer optics. (a) Pinhole focus. The shear plate fringes are parallel to the fiducial line, indicating that the pinhole is at the focus of the collimator. (b) Collimator tilt. The collimator has been tilted to center the collimated beam on the grating. (c) Grating tilt. The grating has been tilted to properly align the red and blue dispersed beams on the focus mirrors. (d) Feedthrough micrometers for tilting the focus mirrors. (e) Focus mirror tilt. Each focus mirror has been tilted to center the pinhole image vertically and properly align the passbands horizontally. (f) Grating rotation. The grating has been clocked so that the broadband image of the pinhole is approximately horizontal in both channels. (g) Slit rotation. The slit has been clocked so that the atmospheric absorption features are approximately vertical in both channels. (h) Cold alignment. Screenshot from the IR visualization software during in-flight alignment of the focus mirrors. The lower panel shows the 3 μm spectral × spatial image and the upper panel a spectral cross section of the image. Spectral alignment is achieved when photospheric absorption features in the measured spectrum (1) overlap with those in the library spectrum (2). Spatial alignment is achieved when light from the slit is centered vertically in the detector, resulting in a dark band at the top (3) and bottom (4).

mount, reducing the slit length by 10% (Figure 9(g)). This issue will be corrected before the 2019 eclipse.

11. *Cold alignment:* The spectrometer was sealed, pumped down, and chilled. As designed, the image focus, spatial rotation, and spectral rotation remained unchanged. The image shifted spectrally and spatially, and this was corrected by tilting the focus mirrors. The final alignment of the focus mirrors was performed in flight, using absorption lines in the solar photosphere to place the spectrum on the detector (Figure 9(h)).

2.3.3. Slit-jaw Camera Alignment

Once the position of the slit-jaw was finalized, the slit-jaw camera was aligned to it. Figure 10 shows the slit-jaw camera and associated optics, with the available adjustments labeled. The slit-jaw itself is out of sight inside the vacuum chamber. The fold mirror was tilted about two axes to center the slit in the image. The plate scale was set by translating the camera and lens as a unit, and the image was focused using the focus adjustment on the camera lens. The target plate scale was $2\farcs31\,\mathrm{pixel}^{-1}$, equivalent to that of the IR camera. Due to limited travel in the translation stage, the maximum available plate scale was $2\farcs26\,\mathrm{pixel}^{-1}$ (Section 3.3.2).

2.3.4. Telescope and Spectrometer Alignment

The telescope was aligned to the spectrometer in tip, tilt, focus, and horizontal and vertical translation. Alignment took place with the spectrometer evacuated, cold, and internally aligned, ensuring that all optical elements were in their flight positions. Tip, tilt, and focus were aligned using a theodolite, and translation was checked using an infrared collimator. Figure 11 shows the alignment scheme and results.

The telescope was placed in its nominal location in front of the spectrometer and fed with a collimated beam from the theodolite. A piece of the theodolite beam was retro-reflected by the telescope alignment cube, allowing the theodolite to be precisely aligned to the telescope LOS. The theodolite output was focused onto the slit-jaw by the telescope and reimaged by the slit-jaw camera (Figure 11(a)).

The telescope was adjusted in tip, tilt, and focus until the image of the theodolite crosshair was centered and focused on the slit (Figure 11(b)). Each time the telescope moved, the theodolite had to be realigned to the telescope alignment cube. This iterative process continued until the center of the theodolite crosshair was less than $1\farcm$ from the center of the slit. In Figure 11(b), the green plus sign marks the center of the slit. The center of the theodolite crosshair is displaced by $40''$.

Next, the infrared image was checked for vignetting resulting from decentering of the telescope pupil on the spectrometer mirrors. Due to diffraction at the slit, the telescope overfilled the spectrometer mirrors horizontally but not vertically. As the vertical direction was more sensitive to decenter, centration was assessed by checking the intensity of the IR image along the slit. The theodolite was replaced with an infrared collimator (Figure 11(a)), which fed the telescope with collimated light

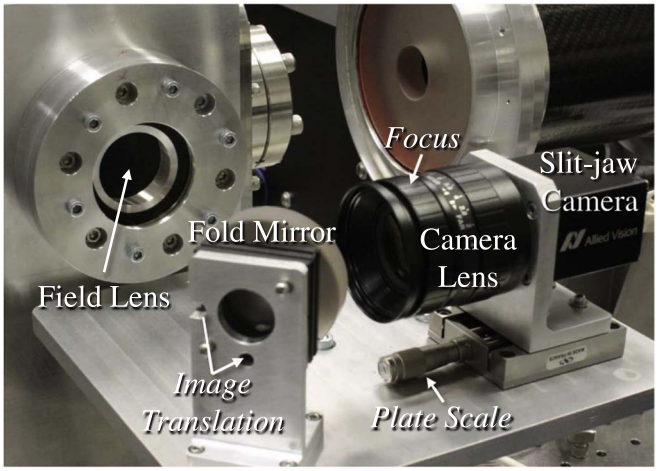

Figure 10. Slit-jaw camera and associated optics.

from a concentric circle target illuminated by a broadband IR lamp. Figure 11(c) shows the slit-jaw image of the target with the slit through the center. Figure 11(d) shows the 4 μm infrared image and the spectrally integrated intensity at each bright circle sampled by the slit. In the intensity plot, variations in the light source have been removed by dividing by the intensity in the slit-jaw image, and the result has been normalized. The intensity is relatively constant along the slit, indicating that the nominal telescope position adequately centered the pupil in the spectrometer mirrors. The slit vignetting discussed in Section 2.3.2 is apparent near the bottom of the intensity plot in Figure 11(d).

2.3.5. Image Stabilization System Alignment

In the final step of the optical alignment, the fiber-optic gyroscope and fast-steering mirror were aligned to the telescope. The three gyroscope axes were referenced by a corner cube aligned to x arcmin using a coordinate measuring machine. Two alignment holes in the bottom surface of the gyroscope package provided a precise reference for the gyroscope axes.

Figure 12(a) shows the alignment of the gyroscope to the telescope. The theodolite was aligned to the telescope LOS by centering its crosshair on the center of the slit. Part of the theodolite beam was retro-reflected by the gyro corner cube. The gyroscope was tilted about its x- and z-axes until the y-axis was aligned to the theodolite and therefore to the telescope LOS. The final alignment error between the gyroscope and telescope was less than 10″ in each axis.

The fast-steering mirror was installed and the theodolite was rotated 90° to feed this mirror (Figure 12(b)). The theodolite was aligned along gyro x using the alignment cube. Using the adjustments in Figure 12(c), the mirror assembly was rotated in azimuth and zenith until the image of the theodolite crosshair was centered at slit center. In this orientation, the fast-steering mirror reflected the theodolite beam from gyro x to gyro y (the telescope LOS), performing a 90° rotation about gyro z. The resulting azimuth and zenith stage positions defined the origin from which all future positions were measured.

2.4. Eclipse Flight

AIR-Spec observed the total eclipse from GV HIAPER between 18:22 and 18:26 UTC. The observation took place over western Kentucky, near maximum duration. The eclipse flight started and ended in Chattanooga, Tennessee, in order to minimize the fuel requirements and allow the Gulfstream V to fly at 14.3 km altitude, as high as possible above the IR-absorbing water vapor. To bring the spectrometer optics to thermal equilibrium, the instrument was cooled with liquid nitrogen beginning 6 hr before takeoff and ending 30 minutes before takeoff.

The flight path was designed to maximize the time spent in totality while optimizing the orientation of the aircraft before and during totality. Before entering the eclipse path, the GV flew a series of headings that compensated for the changing azimuth of the Sun. This allowed the Sun to be acquired well before second contact with the instrument optimally positioned for totality. The predetermined instrument position accounted for the likely wind direction, allowing the GV to fly along the eclipse path while remaining in an orientation that kept the total eclipse in the telescope.

Figure 13 shows the 3 hr eclipse flight. The aircraft took off 2 hr before second contact (18:22 UTC), flew northwest for about 50 minutes, and entered a holding pattern. The partial eclipse began, and the crew began adding dry ice to the IR camera interface. About 25 minutes before totality, the GV exited the holding pattern and the Sun was acquired. The final spectral and spatial alignment was performed as described in Section 2.3.2. AIR-Spec observed totality for 4 minutes, collecting dark frames before and after and photospheric calibration data near the end of the flight. The GV landed in Chattanooga about 45 minutes after totality.

3. The 2017 August 21 Eclipse Data

The carefully planned flight and operations resulted in 4 minutes of data at four positions in the corona, as well as a 5 s observation of the chromosphere (Table 4). All five target lines were observed (Table 5). Prior measurement campaigns have confirmed the existence of Si X at 1.431 μm (Penn & Kuhn 1994; Kuhn et al. 1996), S XI at 1.921 μm (Olsen et al. 1971; Kastner 1993), Mg VIII at 3.028 μm (Münch et al. 1967; Olsen et al. 1971), and Si IX at 3.935 μm (Kuhn et al. 1999; Judge et al. 2002). AIR-Spec made the first detection of Fe IX at 2.853 μm (Samra et al. 2018). Through coordinated observations with the Extreme Ultraviolet Imaging Spectrometer (EIS; Culhane et al. 2007), the AIR-Spec measurements provided insight into line excitation processes and coronal temperature and density (Madsen et al. 2019).

The post-processing scheme includes dark subtraction, defective pixel replacement, and image rectification and registration. Observations of the photosphere are used to calibrate wavelength, pointing, plate scale, throughput, and resolution.

3.1. Summary of Observations

AIR-Spec observed the corona at four positions, sampling the west limb, a solar prominence, and the east limb (including an active region). A fifth position measured the chromosphere at third contact. Table 4 lists the time spent at each position and the number of frames acquired in each camera. Most of totality was spent on the west limb to coordinate with other observatories.

Figure 14 shows the average slit position for each observation superimposed on a composite of images from the

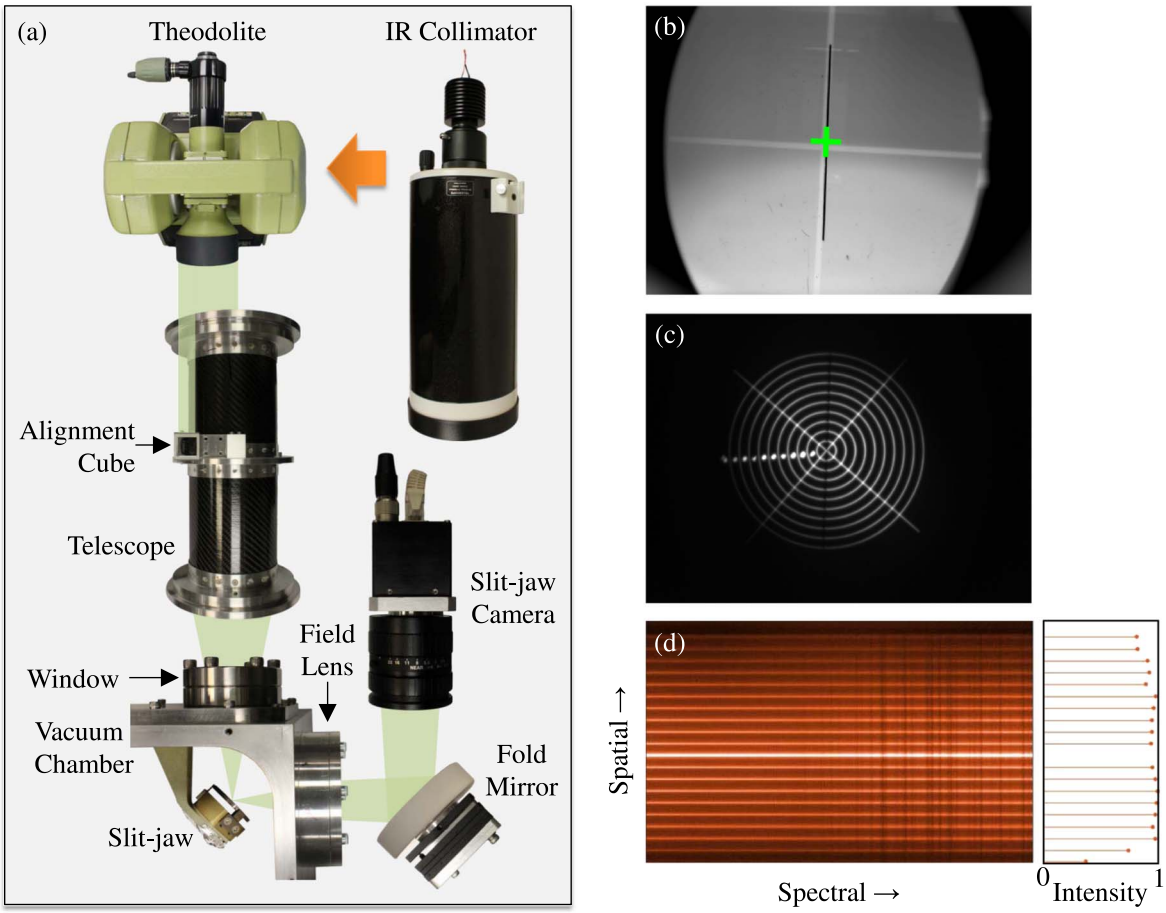

Figure 11. Aligning the telescope to the spectrometer. (a) Diagram of components. The theodolite was used to align tip, tilt, and focus, while the IR collimator was used to check centration. (b) Slit-jaw image of the theodolite crosshair. The green plus sign marks the center of the slit, 40″ from the center of the theodolite crosshair. The slit and theodolite crosshair are both in focus. (c) Slit-jaw image of a concentric circle target from the IR collimator. (d) 4 μm IR image of the concentric circle target. The intensity is uniform over the length of the slit, confirming that the telescope pupil is centered on the spectrometer mirrors.

slit-jaw camera (left) and the mean infrared spectrum corresponding to each slit position (right). Each baseline-subtracted spectrum was averaged completely in time and over 35″ at the limb. Neutral hydrogen was observed in the prominence and chromosphere. Features appearing at 2.843 μm in positions 1–4 and 3.021, 2.854, and 3.873 μm in position 5 are not emission lines but artifacts caused by stray reflections inside the slit-jaw substrate (Samra et al. 2019).

Fe IX was observed in position 3 (east limb), and the other four target lines were observed in all of the coronal positions. Gaussian fits to each coronal line (Figure 15) provided the center wavelength in positions 1–4 (Table 5). Uncertainties in the wavelengths of the observed coronal lines arise from a combination of the error in the Gaussian fits and uncertainties in the wavelength mapping (Table 6).

3.2. Image Processing

Each infrared camera frame was processed to remove the dark background, replace defective pixels, align the spatial and spectral axes with the image, register to other frames along the slit, and remove interference fringes from the 4 μm channel. Fringes were not observed in the 3 μm channel. Two-dimensional image registration was performed on the slit-jaw images.

3.2.1. Dark Subtraction

Because of the significant thermal background discussed in Section 2.2.3, it was necessary to subtract a dark frame from each infrared data frame in order to see the IR corona. Due to the high spatial uniformity of the focal plane (Figure 4), the weakness of the coronal signal compared to the background, and the difficulty of taking flat-field data with the spectrometer at its operating temperature of 150 K, dark subtraction was used in lieu of a flat-field correction. The dark subtraction removes the offset nonuniformity (Figure 4, first panel) and any gain nonuniformity (second panel) associated with the background signal. It cannot remove the gain nonuniformity from the coronal signal, but this residual is insignificant compared to photon noise across the line. The local gain variation of < 0.02 DN/DN (third panel) corresponds to only a few DN on the combined signal from the line and continuum.

Dark frames were collected before and after totality by blocking light from the telescope at the vacuum chamber entrance window. Figure 16 shows the dark frame immediately after totality (panel (a)) and the time variation of the mean dark frame over the 6 minutes following totality (panel (b)). The background image has a mean of about 10,000 DN and significant structure resulting from bright regions inside the spectrometer. In comparison, the measured intensity of the brightest coronal line is about 150 DN. The background

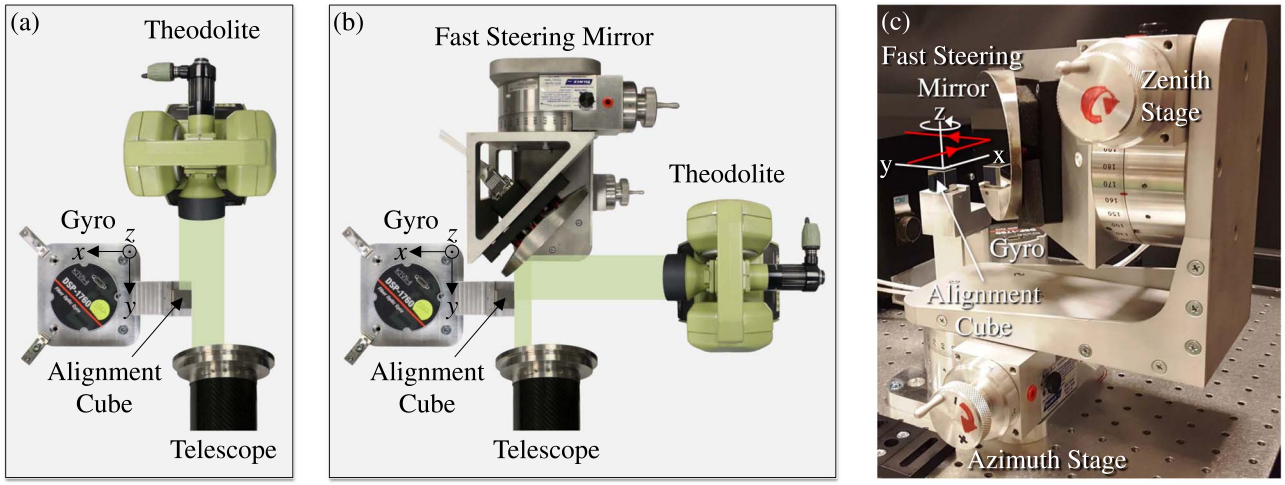

Figure 12. Alignment of the image stabilization system to the telescope. (a) Fiber-optic gyroscope to telescope. (b) Fast-steering mirror to gyroscope and telescope. (c) Fast-steering mirror adjustments.

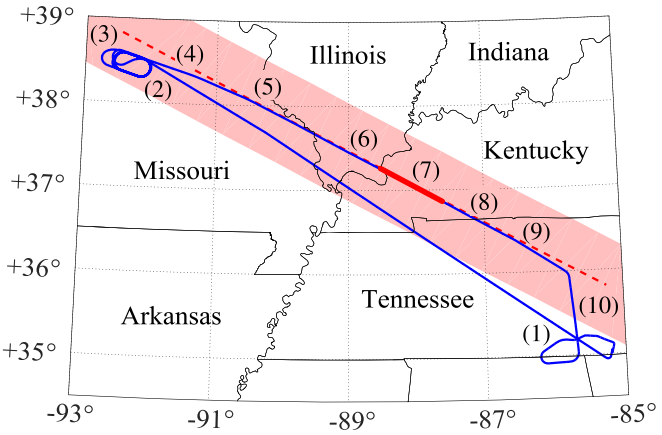

Figure 13. Eclipse flight and operations. The GV flight path is shown in blue, the totality center line is marked by red dashes, and the totality swath appears in light red. The start time of each operation is noted with respect to second contact (C2) at 18:22 UTC. (1) Takeoff from Chattanooga, C2–130 minutes. (2) Enter holding pattern, C2–80 minutes. (3) Begin dry ice, C2–30 minutes. (4) Acquire the Sun, C2–20 minutes. (5) Set wavelength range, C2–10 minutes. (6) Collect darks, C2–2 minutes. (7) Observe totality, C2–0 minutes. (8) Collect darks, C2+4 minutes. (9) Collect calibration data, C2+10 minutes. (10) Land in Chattanooga, C2+45 minutes.

increases with time at a rate of about 80 DN minute^{-1} as the liquid nitrogen evaporates and the dry ice sublimates.

For pixels near the center of the array, a 4.2-minute sinusoidal trend is superimposed on the warm-up. The sine wave comes from the Stirling cooler used to chill the detector. The cold piston of the cooler is in contact with the middle of the focal plane and moves toward and away from the focal plane at 60 Hz, the operating frequency of the cooler. This generates a time-varying acceleration in the pixels near the center of the detector, introducing a piezoelectric effect that changes the intensity in those pixels. The 4.2-minute period is a result of aliasing the 60 Hz fluctuation by sampling at the 15 Hz frame rate. The amplitude A and phase ϕ of the aliased sine wave are given by

$$A = A_0 \sin\left[\pi \ \mathrm{frac}(T_{\mathrm{exp}} \cdot 60\ \mathrm{Hz})\right] \quad (1)$$

$$\phi = \phi_0 + \pi \ \mathrm{frac}(T_{\mathrm{exp}} \cdot 60\ \mathrm{Hz}), \quad (2)$$

Table 4
Summary of the Total Eclipse Observations

Slit Position	Duration	IR Frames	SJ Frames
1. West limb	63.5 sec	953	2083
2. Prominence	41.5 sec	622	1359
3. East limb	35.7 sec	536	1171
4. Prominence and west limb	81.3 sec	1219	2668
5. Chromosphere	5.0 sec	75	164

where "frac" denotes the fractional part of the argument (i.e., the argument modulo 1), T_{exp} is the exposure time, and A_0 and ϕ_0 are the amplitude and phase of the original (unaliased) 60 Hz wave, respectively. A_0 and ϕ_0 vary from pixel to pixel but remain constant in time. They were measured after the eclipse and are shown in panels (a) and (b) of Figure 17.

Because the background varied significantly over the 4 minutes of totality, its time evolution was modeled using an 8-minute series of dark frames from before and after totality. A total of 90 frames (6 s) of data were averaged to produce each sample in the time series. The signal in each pixel was assumed to have the form

$$I(t) = I_0 + r(t - t_0) + a(t - t_0)^2 + A \sin\left(\frac{2\pi(t - t_0)}{4.2\ \mathrm{minutes}} + \phi\right), \quad (3)$$

where I is the pixel intensity in DN, t is the time each frame was collected, t_0 is an arbitrary start time, I_0 is the initial intensity in DN, r is the linear rate of change in DN minute^{-1}, a is the acceleration in DN minute^{-2}, A is the sine wave amplitude in DN, and ϕ is the sine wave phase in radians. A and ϕ were calculated using Equations (1) and (2), and t_0 was selected such that the observed phase of the dark time series was equal to ϕ at $t = t_0$. The sinusoidal term was subtracted from the time series, and I_0, r, and a were estimated for each pixel using a least-squares fit. Maps of I_0 and r are shown in panels (c) and (d) of Figure 17.

Table 5
Measured Wavelengths for the AIR-Spec Coronal Lines

	Si X	S XI	Fe IX	Mg VIII	Si IX
1.	14304.4 ± 2.1 Å	19214.4 ± 0.7 Å		30278.4 ± 3.2 Å	39351.8 ± 1.2 Å
2.	14304.1 ± 2.0 Å	19213.2 ± 0.7 Å		30280.2 ± 2.8 Å	39353.0 ± 1.2 Å
3.	14305.4 ± 1.5 Å	19214.4 ± 0.5 Å	28532.3 ± 3.1 Å	30281.9 ± 2.0 Å	39351.8 ± 0.8 Å
4.	14305.0 ± 1.8 Å	19213.8 ± 0.6 Å		30280.5 ± 2.7 Å	39353.7 ± 1.0 Å

Note. Wavelength estimates and standard errors are reported for each of the four coronal slit positions. The Fe IX line was only seen in position 3 (Samra et al. 2018, 2019). All wavelengths are given in vacuo and have been corrected for solar rotation.

3.2.2. Defective Pixel Replacement

At 60 ms exposure time, defective pixels made up about 2% of the focal plane array. Bad pixels were identified as outliers in the distributions of initial intensity, rate, or acceleration or as pixels with poor fits to Equation (3). They were replaced using bilinear interpolation. Figure 18 shows the histograms for initial intensity (panel (a)), rate (panel (b)), acceleration (panel (c)), and χ^2 (panel (d)), with black vertical lines marking the cutoff values for good pixels. Defective pixels are shown in white in Figure 18(e).

3.2.3. Geometric Correction

After dark subtraction and defective pixel replacement, a geometric correction was applied to remove spectral and spatial shear in the infrared images. Shear arose from the fact that the slit was not parallel to the grating grooves, by design. (The grating was tilted 3°.5 to the slit in the cross-dispersion direction in order to send light to the focus mirrors). The shear is apparent in Figure 19(a), which shows IR data from scattered photospheric light just before totality. The structure along the spectral dimension comes from photospheric and atmospheric absorption, while the spatial structure comes from dust on the slit and variations in the scattered intensity. The spectral shear is more apparent in the image because that dimension is magnified.

Shear was removed by computing a coordinate transformation to align the image axes with the sheared features and then interpolating the data from sheared coordinates to Cartesian coordinates. A gradient filter was used to detect lines along the spectral and spatial features. Each line was defined by two (x, y) coordinate pairs, which were mapped to corrected coordinates (u, v) corresponding to horizontal and vertical lines. Because the sheared lines were straight and parallel, the 2×3 affine transformation T was used to map each (x, y) to (u, v) according to

$$\begin{bmatrix} u \\ v \end{bmatrix} = T \begin{bmatrix} x \\ y \\ 1 \end{bmatrix}. \tag{4}$$

A least-squares estimate for T is given by

$$\hat{T} = UX^T(XX^T)^{-1}, \tag{5}$$

where $U = \begin{bmatrix} u_1 & u_2 & \ldots & u_n \\ v_1 & v_2 & \ldots & v_n \end{bmatrix}$, $X = \begin{bmatrix} x_1 & x_2 & \ldots & x_n \\ y_1 & y_2 & \ldots & y_n \\ 1 & 1 & \ldots & 1 \end{bmatrix}$, and $n \geqslant 3$ is the number of features (lines) extracted. $\hat{T}$ was used to produce a sheared grid aligned with the spectral and spatial features, and the IR data were mapped from the sheared grid to a Cartesian grid using bilinear interpolation. Separate transformations were used to correct the 3 and 4 μm channels. Figure 19(b) shows the IR data after geometric correction. The spectral and spatial features are aligned with the image axes.

3.2.4. Image Registration

In order to remove residual pointing jitter, image registration was performed on frames from both cameras. The slit-jaw images were registered in x, y, and rotation to place solar north up and Moon center at the same location in all frames (Figure 20). The rotation angle was found by comparing the IR corona to the 193 Å channel of the AIA (Lemen et al. 2012), after enhancing features by applying a radial filter and computing the image gradients. Moon center was found by fitting the limb of the Moon to a circle.

The IR images were registered along the spatial dimension by placing the limb of the Moon at the same pixel in all frames. First, each frame was summed along the spectral dimension to produce the integrated intensity at every pixel along the slit. Figure 19(c) shows the spectrally integrated intensity as a function of spatial pixel and time. The inner corona appears as a wavy bright line in each channel, with a sharp intensity change at the limb of the Moon. The spectrally integrated intensity was differentiated with respect to the distance from Sun center, and the pixel with the largest derivative was defined as the limb of the Moon. Each frame was shifted an integer number of spatial pixels to align the location of the limb. Figure 19(d) shows the spectrally integrated intensity after alignment.

3.2.5. Fringe Removal

Interference fringes appeared in the 4 μm channel of the infrared data, due to an etalon effect in the four uncoated sapphire surfaces of the aircraft window. The fringes were oriented vertically on the image and had a period of about 14 pixels (170 μm) and a peak-to-peak amplitude of 5–10 DN, equivalent to about 1.5–3 $\mu B_\odot$ at a wavelength of 3.935 μm. Figure 19(e) shows a sample 4 μm image and its spatial (row) mean. The fringes are bright enough to obscure the two emission lines in the image.

The fringes can be removed by applying a notch filter at the fringe frequency. Figure 21 shows the power spectral density (blue) of the mean row in the 4 μm channel. A peak appears at the fringe frequency of 6 mm^{-1}. The notch filter (black) attenuates frequencies between 5 and 7 mm^{-1}. Figure 19(f) shows the sample 4 μm image after fringe removal. The emission lines are clearly visible. The fringes were not removed in the published data.

3.3. Calibration

The AIR-Spec wavelength, plate scale, pointing, and throughput were calibrated to map spectral pixel to wavelength,

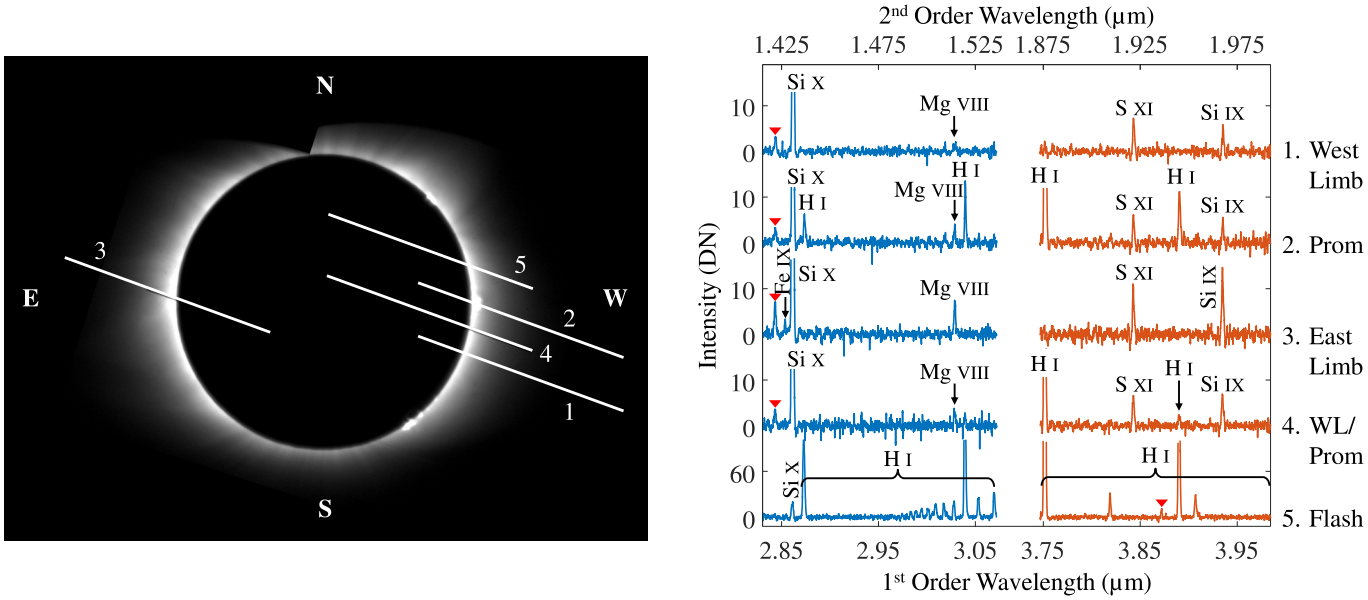

Figure 14. Overview of total eclipse observations. Slit positions superimposed on slit-jaw image (left) and average IR spectra at each slit position (right). Red triangles mark the spectral artifacts.

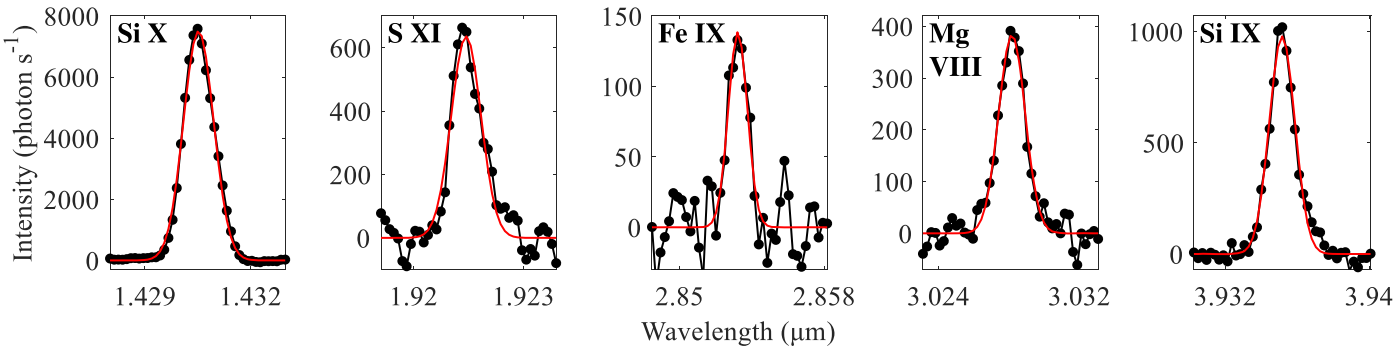

Figure 15. Gaussian fits to the coronal lines in position 3 (east limb active region). The measurements were averaged in time and over the 21 pixels (49″) nearest the lunar limb, corresponding to an average radius of 1.05 $R_{\odot}$.

Table 6
Wavelength Calibration Coefficients and Standard Errors in Slit Position 3

Channel	Start Wavelength (Å)	Dispersion (Å pixel^{-1})
1.5 μm	15359.38 ± 0.98	−1.18338 ± 0.00123
2 μm	19926.94 ± 0.35	−1.16811 ± 0.00048
3 μm	30718.75 ± 1.97	−2.36675 ± 0.00246
4 μm	39853.88 ± 0.71	−2.33622 ± 0.00097

spatial pixel to solar coordinates, and image intensity to spectral radiance. A calibration of the PSF provided a measurement of the spectral and spatial instrument resolution.

3.3.1. Wavelength Calibration

AIR-Spec has a linear mapping from spectral pixel to wavelength. The mapping is constant with respect to spatial pixel (after geometric correction), but it varies in time by more than 4 spectral pixels over the course of the eclipse observation. The start wavelength drifts owing to thermal changes and jitters owing to vibration from the aircraft and camera chiller, while the dispersion remains fixed in time. The temporal trends are different in the two channels, suggesting that the two focus mirrors are the main source of the variations.

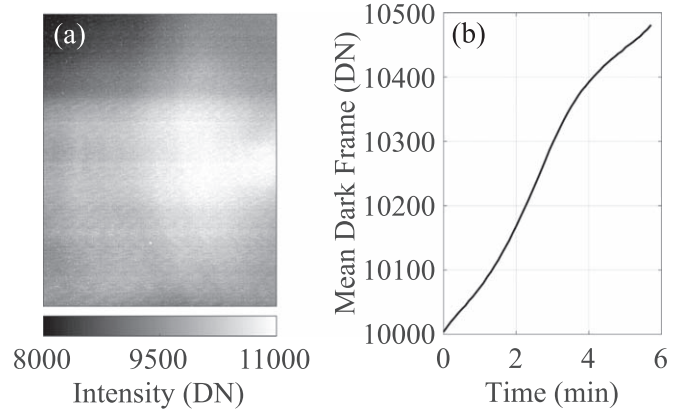

Figure 16. Behavior of the dark background at 60 ms exposure time. (a) Dark frame at the end of totality. (b) 6-minute time series of the spatial average.

These temporal variations in start wavelength can be calibrated as long as they happen on timescales longer than one exposure. This is the case for the thermal drift and the aircraft-related jitter. High-frequency vibration, likely due to the camera chiller, cannot be removed and causes a double peak or broad peak in many of the line observations, especially

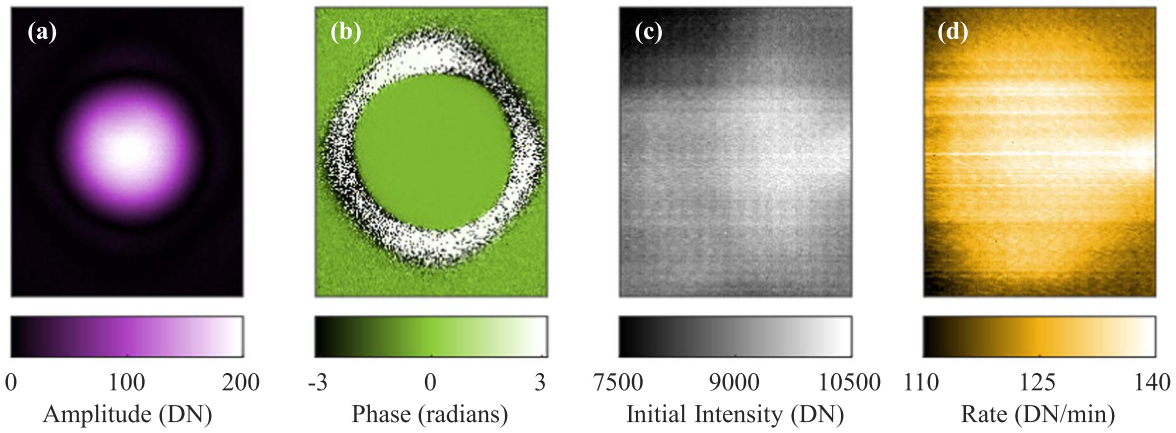

Figure 17. Fit parameters for the time evolution of the dark background. (a) Initial intensity in DN. (b) Rate of change in DN minute^{-1}. (c) Sine wave amplitude in DN. (d) Sine wave phase in radians.

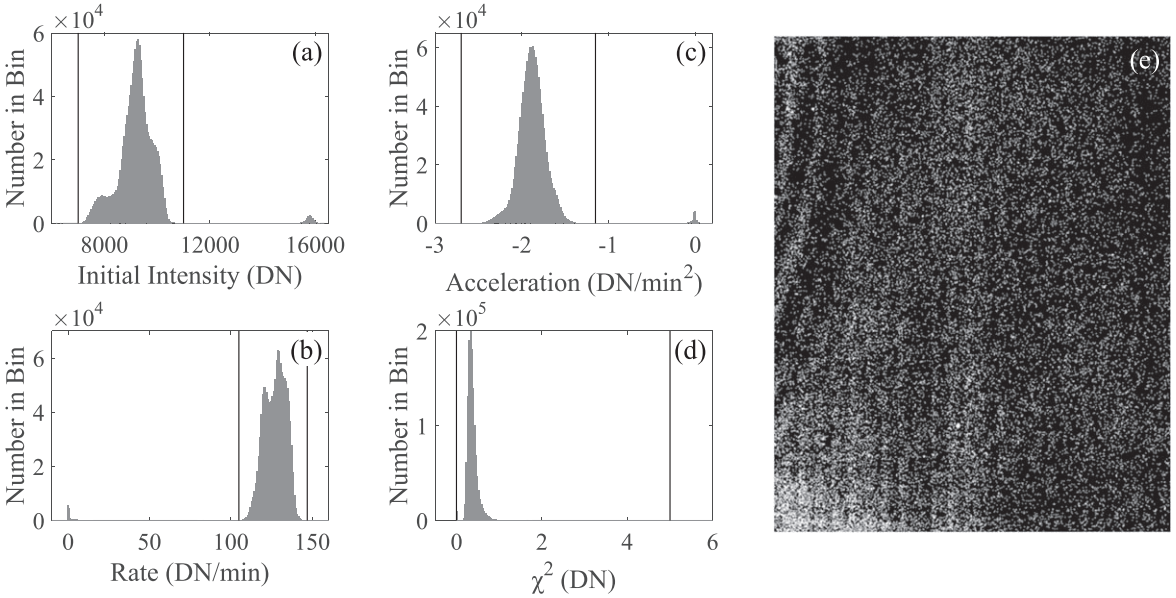

Figure 18. Defective pixels. Histograms are used to identify outliers in (a) initial intensity, (b) rate, (c) acceleration, and (d) goodness of fit. Good pixels lie between the black vertical lines. (e) Defective pixel map. Bad pixels are shown in white and make up 2% of the array.

in the 3 μm channel. This effect appears because the tip/tilt mounts for the focus mirrors are not sufficiently constrained. It reduces the effective spectral resolution and increases the uncertainty in the line wavelengths in Table 5.

Wavelength calibration took place in two steps: first the absolute time-averaged wavelength was calibrated for each slit position, and then the wavelength axis was shifted at each time step to account for the variation in start wavelength. In the coronal slit positions (1–4), the average wavelength mapping was estimated by comparing AIR-Spec's measurement of telluric absorption in the scattered continuum with the ATRAN atmospheric model (Lord 1992), available online at https://atran.arc.nasa.gov. The modeled atmosphere was smoothed to the AIR-Spec resolution, and a nonlinear curve fitting routine was used to stretch and shift the measured data to achieve the best match to the model. In the chromospheric observation (position 5), the time-averaged wavelength was estimated by fitting the hydrogen lines with Gaussians and then doing a linear fit from center pixel to rest wavelength. Table 6 lists the time-averaged wavelength mapping coefficients and their uncertainties for slit position 3 (east limb).

After estimating the average wavelength axis for each slit position, the strong lines Si X 1.431 μm and H I 1.876 μm were used as tracers for the time-varying wavelength offset in the 3 and 4 μm channels. The line measurements were summed to 0.9 s effective exposure time and fit with Gaussians to provide the line centers as a function of time. Each line center time series was modeled as a linear combination of yaw, pitch, roll, their temporal derivatives, and time, resulting in a residual offset of less than 1 pixel over the duration of the total eclipse (Figure 22). These models were then used to predict the 3 and 4 μm start wavelength for every frame.

3.3.2. Plate-scale Measurement and Pointing Calibration

The slit-jaw camera plate scale and slit length were measured using a solar observation from 2 days before the eclipse. The solar diameter was measured by fitting the limb of the disk (Figure 23(a)), and the plate scale and slit length were found to be $2\farcs26$ pixel^{-1} and 1.55 $R_\odot$, respectively. The effective slit length was 10% shorter because the slit-jaw mount clipped light from the slit, as mentioned in Section 2.3.2.

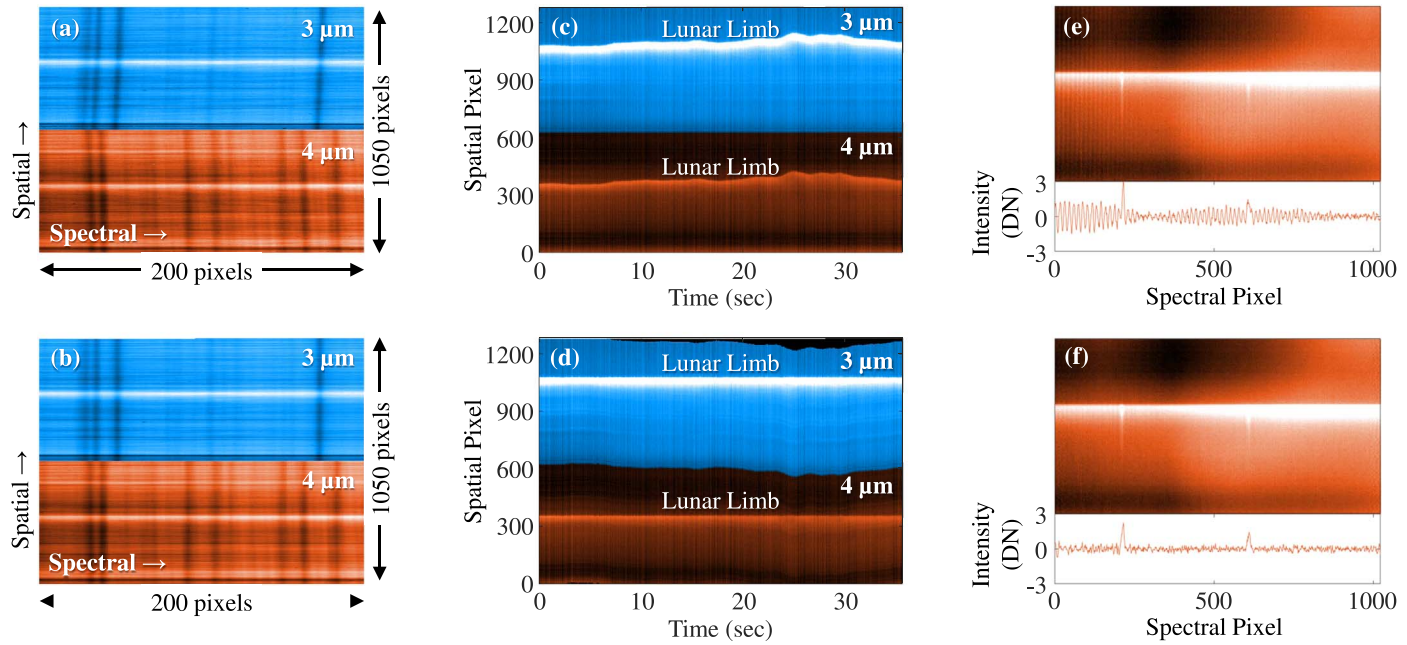

Figure 19. IR image processing: geometric correction, image registration, and fringe removal. The 3°.5 angle between the slit and the grating grooves shears spectral and spatial features with respect to the detector (panel (a)). After geometric correction, the spectral and spatial axes are aligned with the detector axes in both channels (panel (b)). Due to pointing jitter, the lunar limb crosses the slit at a different place in each frame (panel (c)). The high-contrast limb is used to detect the jitter, and each frame is shifted an integer number of pixels to align with the others (panel (d)). In the 4 μm channel, interference fringes obscure the emission lines (panel (e)). The fringes are removed using a notch filter at the fringe frequency (panel (f)).

The IR camera plate scale was computed by comparing simultaneous observations of the partial eclipse in the slit-jaw camera (Figure 23(b)) and IR camera (Figure 23(c)). From the width of the intensity profiles along the slit, the IR plate scale was found to be 2% larger than that of the slit-jaw camera. The IR camera achieved the designed plate scale of $2\farcs31$ pixel^{-1}, while the slit-jaw camera was restricted by the range on its translation stage, as described in Section 2.3.3.

The plate scales were used to map spatial pixels to helioprojective-Cartesian coordinates in both sets of images. Once the slit-jaw frames were aligned with respect to Moon center as described in Section 3.2.4, the solar coordinates of each pixel were computed by accounting for the drift of the Moon relative to the Sun. The time-varying offset between Sun center and Moon center was computed by cross-correlating on a solar prominence over the 4-minute observation. In each IR image, the spatial pixel of the lunar limb crossing was determined using the method explained in Section 3.2.4. The limb crossing was mapped to solar coordinates using the corresponding slit-jaw image, and the coordinates for the other spatial pixels were determined using the IR plate scale.

3.3.3. Throughput Calibration

We define throughput as the product of overall optical efficiency, geometric area of the telescope entrance aperture, slit width in wavelength units, and solid angle subtended by a pixel. The AIR-Spec throughput was estimated using both a bottom-up model and a top-down measurement. The forward model (dashed lines in Figure 24) was computed by simply multiplying the slit width, solid angle, and geometric area from the optical design by the estimated efficiency of each element in the optical train, from the aircraft window to the bandpass filter immediately in front of the detector. We estimate a total optical efficiency (without QE) of about 20% in the 1.5 μm channel, 10% in the 2 μm channel, 35% in the 3 μm channel, and 25% in the 4 μm channel. The grating (20%–80% reflectivity) and the aircraft viewport (70% transmission) are the largest individual contributors to the efficiency estimate.

The top-down throughput calibration relied on photospheric measurements acquired during a test flight 4 days before the eclipse. In order to separate the contributions from first and second order, bandpass filters were used to isolate light near 1.5, 2, 3, and 4 μm. All observations were acquired with a broadband solar filter (transmission $\approx 10^{-3}$) in place. The AIR-Spec data were compared with the expected spectrum at the entrance to the instrument, which was taken as the product of the radiance from the photosphere, the transmission through Earth's atmosphere, and the transmission through the bandpass and solar filters. The photospheric library spectrum came from a combination of ground-based (Wallace et al. 1996) and space-based (Farmer & Norton 1989) measurements and a model from R. Kurucz (http://kurucz.harvard.edu/stars/Sun). The ATRAN model (Lord 1992) was used to provide an estimate of the atmospheric transmission. The transmission of each filter was measured by J. Hannigan of NCAR Atmospheric Chemistry Observations and Modeling using a laboratory Fourier transform spectrometer (FTS).

The throughput was measured as a function of wavelength by fitting a smoothing spline to the quotient of the measured spectrum and library spectrum. The result is shown by the solid lines in Figure 24. Figure 25 shows the agreement between the AIR-Spec data and library spectrum after the latter was multiplied by the throughput and first and second order were summed together.

The measured throughput estimate is 2–3 times smaller than the modeled estimate (Figure 24). We are still exploring possible causes for this discrepancy, but we suspect a combination of factors: (1) The geometric area of the instrument was probably slightly smaller than designed owing

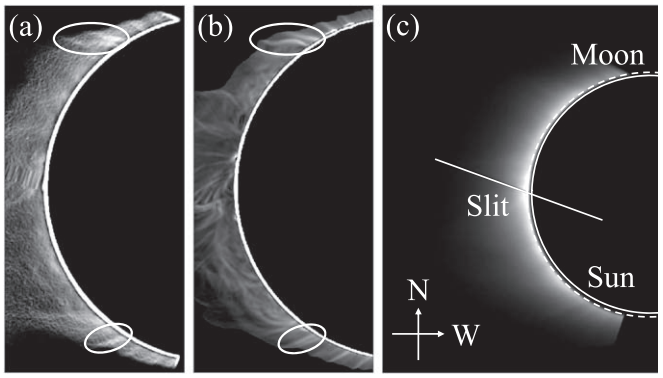

Figure 20. Slit-jaw image registration. By matching features in (a) AIR-Spec and (b) AIA 193, the slit-jaw frames are rotated to orient solar north up. Moon center is found by fitting the lunar limb to a circle (panel (c)). Each frame is shifted horizontally and vertically to place Moon center in the same location.

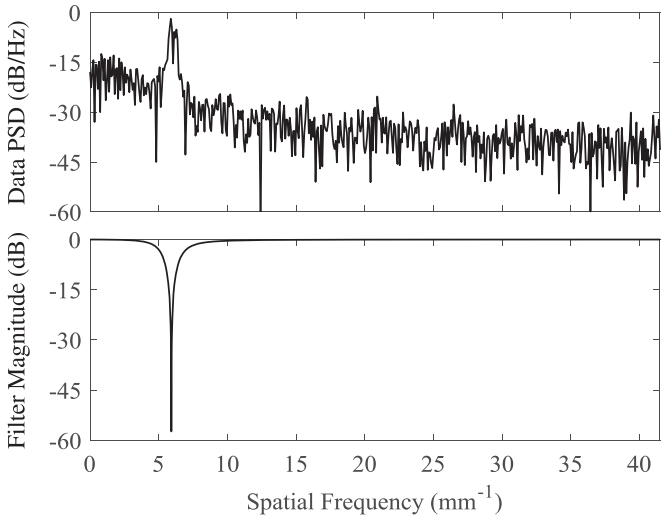

Figure 21. Power spectral density of the mean row in the 4 μm channel (top). Fringes with a period of 14 pixels (170 μm) appear as a peak at 6 mm^{-1}. The notch filter (bottom) attenuates frequencies between 5 and 7 mm^{-1}, removing the fringes.

to the angle of the Sun on the feed mirror and misalignments inside the spectrometer. (2) When the highly attenuating solar filter was placed into the FTS path to measure its transmission, it was necessary to increase the aperture diameter and preamplifier gain to produce a measurable signal at the FTS detector. The change in settings adds some uncertainty to the transmission measurement. (3) The photospheric AIR-Spec measurements may have been influenced by limb darkening, in which case the library spectrum would have overestimated the intensity of the photosphere. (4) For optical elements without transmission/reflectivity measurements, we based our efficiency estimates on the typical performance specified by the manufacturer. This likely resulted in an overestimate of the overall efficiency. In the future, we will use a calibrated lamp to measure throughput in the laboratory, where we have fewer sources of error and greater control over the experimental conditions.

Based on our understanding of the AIR-Spec alignment and the linearity of the FTS used to measure filter transmission, we believe that the first two factors together are responsible for <20% of the measured-modeled throughput discrepancy. In addition, these errors cannot explain the wavelength

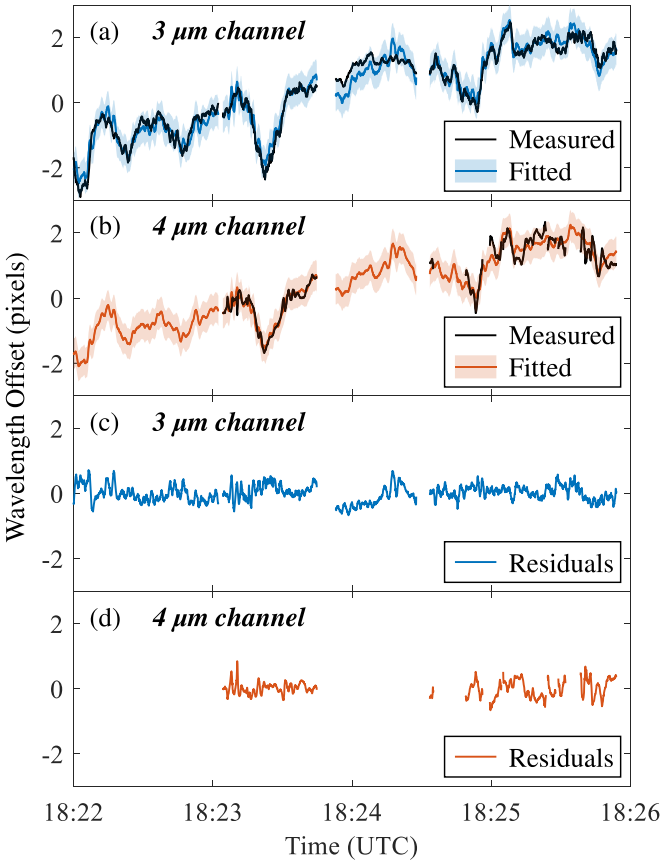

Figure 22. Modeling wavelength drift/jitter as a linear combination of attitude and time. Measurements and fit for (a) the 3 μm channel and (b) the 4 μm channel. The shaded regions are the 95% prediction intervals. Fit residuals for (c) the 3 μm channel and (d) the 4 μm channel.

dependence of the discrepancy. We also expect limb darkening to contribute no more than 20% of the difference, as the average intensity across the solar disk is about 80% of the intensity at the center at 500 nm wavelength. We believe that at least 50% of the discrepancy can be explained by overestimates of the individual optical efficiencies, especially the reflectivity of the protected-silver coating on the fast-steering mirror. This coating degraded significantly between delivery and flight, but the mirror was an integrated unit that could not be easily recoated without impact to the tight schedule.

3.3.4. PSF Measurement

The AIR-Spec PSF was measured using an observation of the photosphere immediately after third contact. At the time of the observation, the exposed photosphere was a bright point source, and a single frame at an exposure time of 0.3 ms provided a high-S/N measurement of the resolution in both channels. The raw data are shown in Figure 26. The photosphere appears as a bright line spanning all wavelengths but only a few spatial pixels.

The PSF FWHM was measured by fitting a Lorentzian to the data in each spectral channel. The FWHM is plotted as a function of wavelength in Figure 27. Due to the optical design, the PSF is about 1 pixel broader in the 4 μm channel than in the 3 μm channel. The FWHM of 4.8–5.6 pixels corresponds to a spatial resolution of 11″–13″ and a spectral resolution of about 14–15 Å in first order (half that value in second order), once the effect of the slit is included. Measurements of a narrow, bright

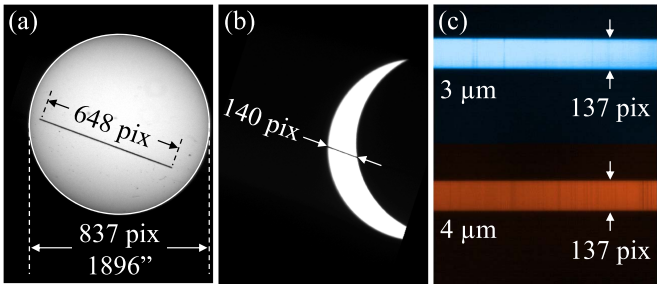

Figure 23. Measuring plate scale. The slit-jaw camera plate scale and slit length are calculated experimentally by fitting the limb of the solar disk to measure its diameter (panel (a)). The plate scale is $2\farcs26$ pixel^{-1}, and the slit length is 1.55 $R_\odot$. The IR camera plate scale is computed by comparing simultaneous observations of the partial eclipse in the slit-jaw camera (panel (b)) and IR camera (panel (c)). The IR camera has a plate scale of $2\farcs31$ pixel^{-1}, 2% larger than the slit-jaw camera.

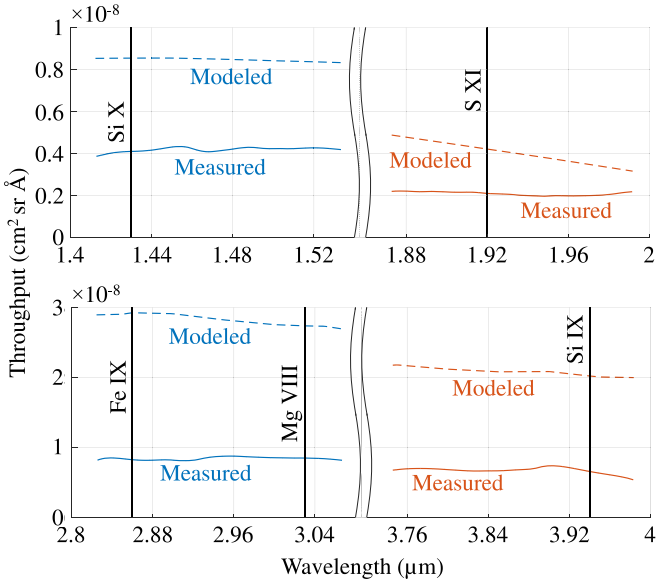

Figure 24. Measured and modeled throughput.

hydrogen line (H I 1.876 μm) confirm the value for spectral resolution. In the 3 μm channel, the effective spectral resolution is broadened up to 50% by the high-frequency wavelength jitter described in Section 3.3.1.

3.4. Data Description

The AIR-Spec data have been organized by slit position into five separate observations (Table 4) and are available on the Virtual Solar Observatory at https://nso.virtualsolar.org/AIR-Spec/. Each data set consists of three 3D arrays with images from the slit-jaw camera and 3 μm/4 μm channels of the IR camera, as depicted in Figure 28.

All slit-jaw frames have been aligned with respect to Moon center and rotated to orient solar north up. Each data point is indexed by solar coordinates and time. The solar coordinates are different for every frame because the Moon drifts with respect to the Sun. Solar x is fixed over rows but varies with column and frame. Solar y is fixed over columns but varies with row and frame. Time is fixed over rows and columns but varies with frame.

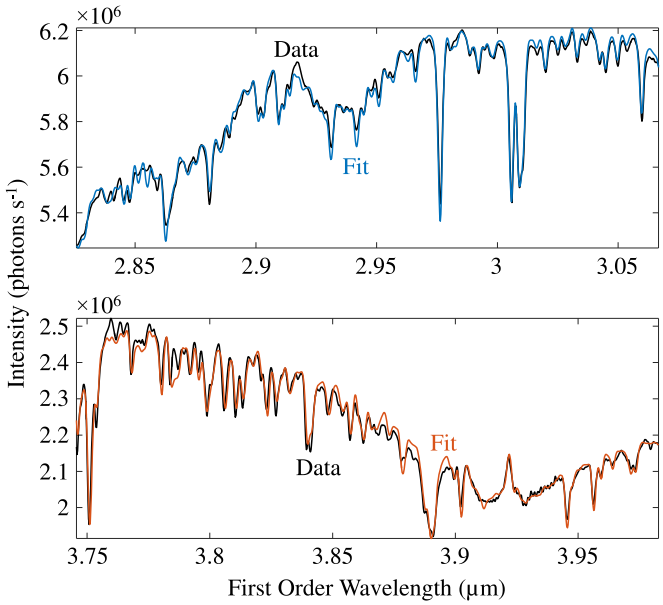

Figure 25. Checking the inverse-modeled throughput. The black line is AIR-Spec data, converted from DN (1 DN = 3.25 e$^-$) to photons s^{-1}. The red line shows the photospheric library spectrum after multiplication by the inverse-modeled throughput.

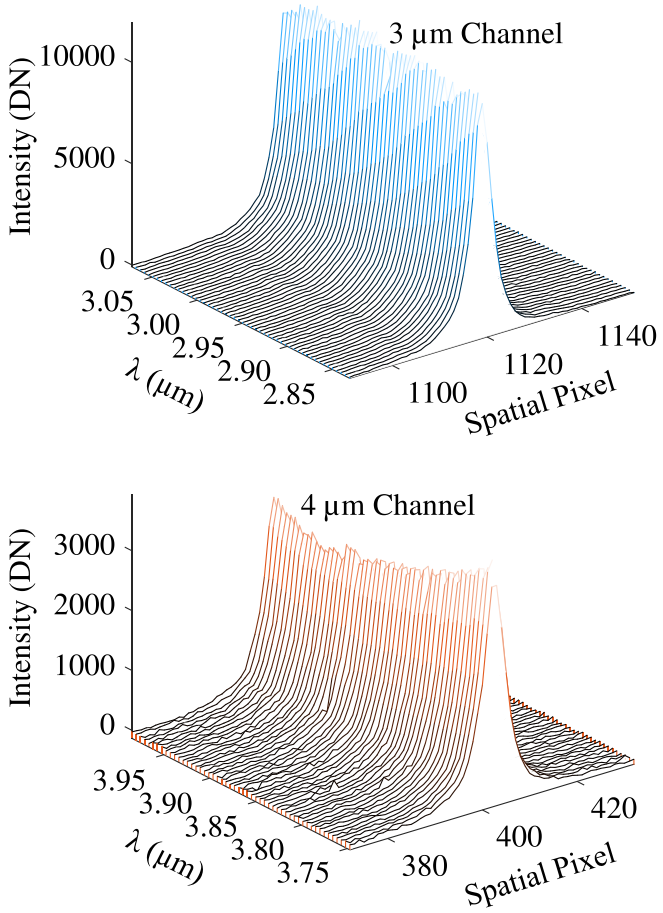

Figure 26. Measuring PSF.

All IR frames have undergone dark subtraction, defective pixel replacement, and geometric correction. Frames have been co-aligned spatially so that the limb crossings coincide. Each

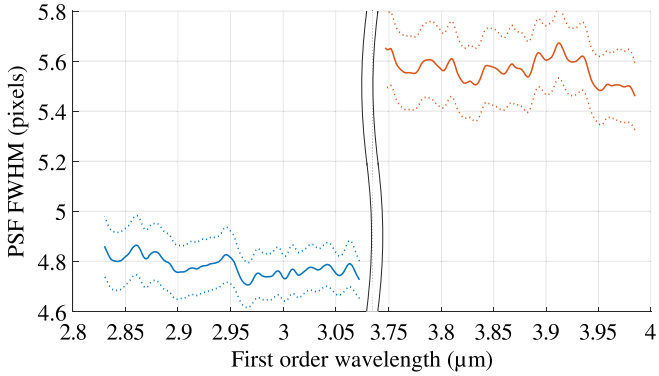

Figure 27. PSF FWHM across the detector. The dotted lines represent 95% confidence intervals.

data point is indexed by solar coordinates, wavelength, and time. Solar x and y are fixed over spectral pixel but vary with spatial pixel and frame. Wavelength is fixed over spatial pixel but varies with spectral pixel and frame. Time is fixed over spatial and spectral pixel but varies with frame.

4. Future Instrument Improvements

The 2017 AIR-Spec observations suffered from three limitations: (1) high thermal instrument background, including significant spatial structure and temporal variations; (2) substantial image jitter; and (3) ghost and double-peak spectral artifacts due to stray reflections in the slit-jaw substrate (Samra et al. 2019) and insufficient constraints on the focus mirror mounts, respectively. We discovered the spectral artifacts and temporal variation of the instrument background during analysis of the 2017 data. We were aware of the thermal background and image stability issues before the eclipse, but the tight schedule did not permit us to improve the instrument in time to make the observation. We made the decision to observe anyway because we were confident that we would measure the strong Si X line and hopeful that we might measure or place an upper limit on the intensities of the other four target lines. Ahead of the 2019 eclipse, we made significant improvements and corrected all of the above issues. Samra et al. (2021) explain the improvements in detail.

The camera was returned to the manufacturer for an upgrade that included a new band-limiting filter with 3 μm cutoff (resulting in the loss of the 3.935 μm Si IX line), improved baffling to block light from the warm window mount, and a lower focal plane temperature of 50 K to reduce the dark current. Altogether, this resulted in a 30$\times$ reduction in the instrument background during the 2019 eclipse. By blocking light at 4 μm, the new filter had the unintended positive consequence of removing the interference fringes from the 4 μm channel. The background temporal variation was removed by minimizing the time between the end of one exposure and the start of the next frame (setting the exposure time as close as possible to the inverse frame rate). A 5$\times$ reduction in image jitter was achieved by adding real-time closed-loop feedback to the image stabilization system to supplement the feedforward signal from the gyroscope. The closed-loop error signal was computed by fitting a circle to the lunar limb in the slit-jaw camera. The stray slit-jaw reflections were blocked with a metal shield added to the back of the sapphire substrate, and the focus mirror mounts were better constrained, completely eliminating the broad/double-peak line shape artifacts.

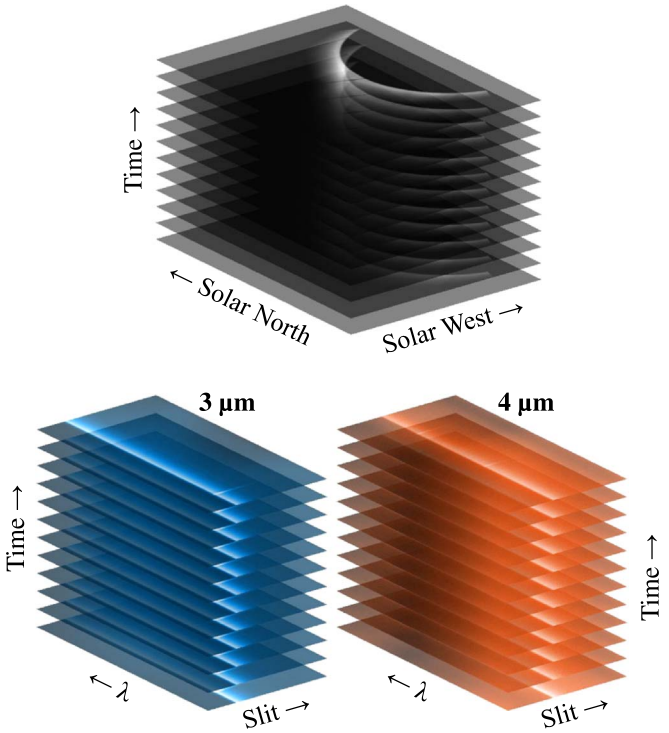

Figure 28. Illustration of data from one of the five eclipse observations. The data set consists of three 3D arrays from the slit-jaw camera and both channels of the IR camera.

AIR-Spec would never have been conceived without Philip Judge of the NCAR High Altitude Observatory (HAO), whose theoretical work laid the foundation for the eclipse observation. Phil provided invaluable guidance as we planned the experiment and interpreted the results. We are very grateful for his help in making AIR-Spec a success. We gratefully acknowledge SAO colleagues Roger Eng, Sam Fedeler, Tom Gauron, Kim Goins, Giora Guth, Stan Kench, Joyce Medaglia, Brian Robertson, and Dave Weaver for their help in creating AIR-Spec. We thank Louis Lussier and the team at the NCAR Research Aviation Facility (RAF) for enabling the Gulfstream V flights; Stuart Beaton of NCAR RAF for specifying, purchasing, and sharing information on the sapphire viewport; Steven Tomczyk of NCAR HAO for lending his equipment, optical expertize, and laboratory space; and Giulio Del Zanna, Helen Mason, Serge Koutchmy, and Shadia Habbal, whose expertize in spectroscopy helped us plan the experiment and interpret the data. We thank Robert Kurucz of SAO for providing a photospheric spectrum for the wavelength and radiometric calibrations and Brian McLeod and Giovanni Fazio of SAO for sharing their expertize in the design and implementation of infrared systems. Finally, we thank the anonymous reviewer for suggesting a number of changes that improved the clarity and completeness of this paper. The development of AIR-Spec was made possible by a National Science Foundation Major Research Instrumentation grant, AGS-1531549, with support shared by Smithsonian Institution. J.W.H. is supported by NASA contract NNX17AE38G.

ORCID iDs

Jenna E. Samra https://orcid.org/0000-0002-4498-8706
Vanessa Marquez https://orcid.org/0000-0001-5388-3298
Edward E. DeLuca https://orcid.org/0000-0001-7416-2895
Leon Golub https://orcid.org/0000-0001-9638-3082
James W. Hannigan https://orcid.org/0000-0002-4269-1677
Chad A. Madsen https://orcid.org/0000-0001-8775-913X
Alisha Vira https://orcid.org/0000-0003-0869-4951
Arn Adams https://orcid.org/0000-0003-2237-0670

References

Casini, R., & Judge, P. G. 1999, ApJ, 522, 524
Contesse, L., Koutchmy, S., & Viladrich, C. 2004, AnGeo, 22, 3055
Culhane, J. L., Harra, L. K., James, A. M., et al. 2007, SoPh, 243, 19
Del Zanna, G., & DeLuca, E. E. 2018, ApJ, 852, 52
Farmer, C. B., & Norton, R. H. 1989, A high-resolution atlas of the infrared spectrum of the sun and the earth atmosphere from space. A compilation of ATMOS spectra of the region from 650 to 4800 cm-1 (2.3 to 16 μm). Vol. I. The sun. RP-1224, NASA
Habbal, S. R., Druckmüller, M., Morgan, H., et al. 2011, ApJ, 734, 120
Judge, P., Casini, R., Tomczyk, S., Edwards, D. P., & Francis, E. 2001, Coronal Magnetogmetry: A feasibility study NCAR/TN-446+STR, Univ. Corporation for Atmospheric Research
Judge, P. G. 1998, ApJ, 500, 1009
Judge, P. G., Tomczyk, S., Livingston, W. C., Keller, C. U., & Penn, M. J. 2002, ApJL, 576, L157
Kastner, S. O. 1993, SoPh, 143, 197
Kuhn, J. R., MacQueen, R. M., Streete, J., et al. 1999, ApJ, 521, 478
Kuhn, J. R., Penn, M. J., & Mann, I. 1996, ApJL, 456, L67
Lemen, J. R., Title, A. M., Akin, D. J., et al. 2012, SoPh, 275, 17
Lin, H., & Casini, R. 2000, ApJ, 542, 528
Lord, S. D. 1992, A New Software Tool for Computing Earth's Atmospheric Transmission of Near- and Far-Infrared Radiation 103957, NASA, https://ntrs.nasa.gov/citations/19930010877
Madsen, C. A., Samra, J. E., Del Zanna, G., & DeLuca, E. E. 2019, ApJ, 880, 102
Münch, G., Neugebauer, G., & McCammon, D. 1967, ApJ, 149, 681
Olsen, K. H., Anderson, C. R., & Stewart, J. N. 1971, SoPh, 21, 360
Penn, M. J. 2014, LRSP, 11, 2
Penn, M. J., & Kuhn, J. R. 1994, ApJ, 434, 807
Pontieu, B. D., & McIntosh, S. W. 2010, ApJ, 722, 1013
Rimmele, T. R., Warner, M., Keil, S. L., et al. 2020, SoPh, 295, 172
Samra, J. E., Judge, P. G., DeLuca, E. E., & Hannigan, J. W. 2018, ApJL, 856, L29
Samra, J. E., Judge, P. G., DeLuca, E. E., & Hannigan, J. W. 2019, ApJL, 873, L25
Samra, J. E., Madsen, C. A., Cheimets, P., et al. 2022, ApJ, 933, 82
Tomczyk, S., McIntosh, S. W., Keil, S. L., et al. 2007, Sci, 317, 1192
Tritschler, A., Rimmele, T. R., Berukoff, S., et al. 2016, AN, 337, 1064
Wallace, L., Livingston, W., Hinkle, K., & Bernath, P. 1996, ApJS, 106, 165
Zygo Corporation. 2015, ZYGO's Guide to Typical Interferometer Setups SB-0205D, https://www.zygoserver.com/met/setupsguide/interferometer-setups.pdf